

Detailed nuclear structure calculations for coherent elastic neutrino-nucleus scattering

Raghda Abdel Khaleq,^{1,2,3,*} Jayden L. Newstead,^{4,†} Cedric Simenel,^{1,2,3,‡} and Andrew E. Stuchbery^{2,3,§}

¹*Department of Fundamental and Theoretical Physics,
Research School of Physics, Australian National University, ACT, 2601, Australia*

²*Department of Nuclear Physics and Accelerator Applications, Re-
search School of Physics, Australian National University, ACT, 2601, Australia*

³*ARC Centre of Excellence for Dark Matter Particle Physics, Australia*

⁴*ARC Centre of Excellence for Dark Matter Particle Physics,
School of Physics, The University of Melbourne, Victoria 3010, Australia*

Any discovery of ‘new physics’ in the neutrino sector first requires a precise prediction of the expected Standard Model cross section. Currently, Coherent Elastic neutrino-Nucleus Scattering (CEvNS) experiments are statistics limited. However, as new and future experiments scale up, it will be necessary to improve the theoretical predictions. Here we review the calculation of the CEvNS cross section in a consistent theory of hadronic currents and compute the relevant nuclear form factors using the nuclear shell model. The uncertainty on the form factors is explored by repeating the calculation for various shell model interactions and with Skyrme-Hartree-Fock evaluations of the Weak-charge radii. We then refine the Standard Model predictions for the recent experimental results of the COHERENT experiment. We find that our cross sections are in good agreement with previous predictions, but with significantly smaller uncertainties - by up to a factor of 10. Near-future CEvNS experiments will meaningfully benefit from improved predictions through an increased sensitivity to new-physics signals.

I. INTRODUCTION

The elastic scattering of neutrinos from nuclei via the weak neutral current is a process that can experience a coherent enhancement at sufficiently small momentum transfer. Dubbed CEvNS, the coherent enhancement of this process boosts the cross section by orders of magnitude, making it much larger than other processes involving neutrinos. This enhancement would suggest that the process should be relatively easy to observe, however the observational signature, a low-energy nuclear recoil, is very difficult to detect. Steady advancement in detector technology enabled CEvNS to finally be observed in 2017.

The first detection of neutrinos via CEvNS was performed by the COHERENT experiment using a small (14.6 kg) cesium-iodide detector [1]. This measurement was quickly followed up by a detection using a liquid argon detector [2]. The next planned measurement will be with an array of germanium detectors (18 kg) [3]. All of these measurements were carried out at the Spallation Neutron Source (SNS) at Oak Ridge National Laboratory. There, neutrinos with energies up to ~ 50 MeV are created from pions decaying at rest within the mercury spallation target. Together, these measurements have observed hundreds of CEvNS events and are broadly consistent with the Standard Model expectation for the process.

CEvNS has many potential applications, both prac-

tical and fundamental. While the practical applications, such as nuclear reactor monitoring [4], require further detector development before they can be realized, advances in nuclear [5–7] and fundamental physics are already being realized with current experiments [8–11]. Notably, CEvNS experiments are the leading probe of some realizations of sterile neutrinos and non-standard neutrino interactions [12]. CEvNS could be detected in dark matter experiments and potentially provide the first warning of a supernova signal [13]. Key to maximising the effectiveness of these applications is having precise predictions for the scattering rate. That is, if one is interested in detecting deviations from the Standard Model at the sub-percent level, then a commensurate level of precision is required for the theoretical predictions.

The dominant systematic uncertainty in CEvNS rate predictions comes from the neutrino flux, which is presently $\sim 10\%$. However, future dedicated measurements by COHERENT will reduce this significantly [14], with the eventual goal of being at the \sim percent level. Relatively little attention has been given to the theoretical uncertainties of the cross section. With CEvNS being a low-energy process, it is generally possible to make approximations to the cross section calculation without significantly sacrificing the accuracy. For example, nuclear structure effects are only accounted for through a single density form factor. Recently, the cross section calculation has been revisited and a modern accounting of nucleon currents applied [15]; however, it is not yet used widely. There has also been a first principles calculation using coupled cluster theory, however it only applies to argon [16]. Additionally, there has been renewed interest in the inelastic neutral-current scattering calculations [17, 18].

In this work we calculate the CEvNS cross sections for

* Raghda.AbdelKhaleq@anu.edu.au

† jnewstead@unimelb.edu.au

‡ cedric.simenel@anu.edu.au

§ andrew.Stuchbery@anu.edu.au

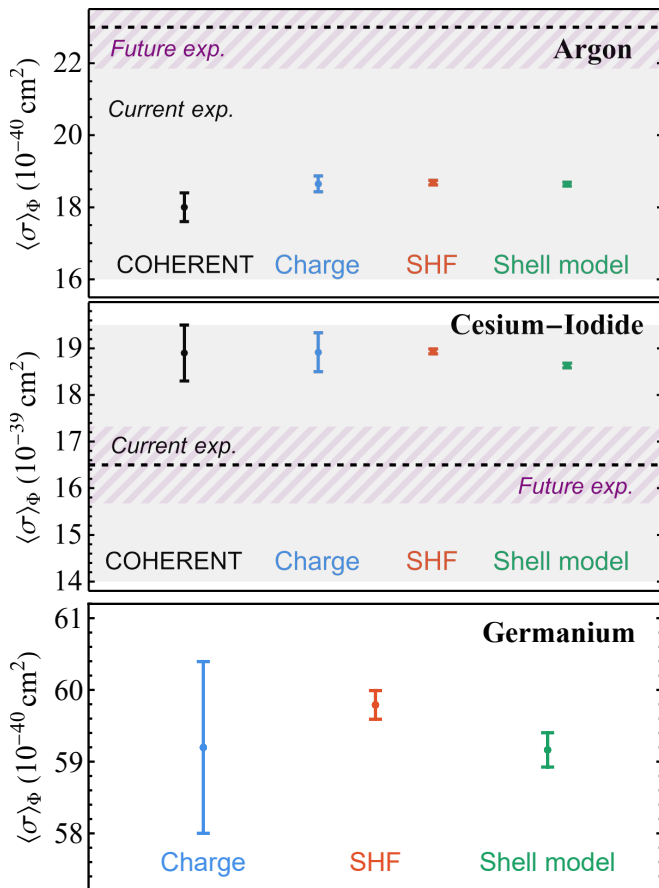


FIG. 1: Theoretical predictions of SNS-flux averaged cross sections for the three targets considered in this work. Shown are our main results using the shell model and Skyrme-Hartree-Fock (SHF) and comparisons with the Klein-Nystrand form factor (using electric charge radii) and COHERENT’s prediction. Also shown is COHERENT’s experimental result (black dashed, with gray region showing uncertainty), and a potential future measurement with 5% error (purple hatched).

nuclear targets used by COHERENT, including the nuclear structure effects, which are typically ignored. To this end, we use large-scale nuclear shell model calculations to derive all relevant nuclear form factors. Using several different nuclear Hamiltonians, we evaluate the uncertainty in the cross section from the nuclear structure effects. These results are then applied to improve the theoretical predictions of the CEvNS event rates that COHERENT has observed to date.

II. CEVNS CROSS SECTION

Shortly after the discovery of Weak neutral currents in 1973, it was suggested that this interaction should coherently enhance the scattering of neutrinos from the nucleus [19]. At very low momentum transfer, q , where q is

less than the inverse size of the nucleus, the cross section approximately scales with the number of neutrons in the nucleus. For neutrinos with energies of tens of MeV, the momentum transfer can be large enough to probe the internal structure of the nucleus, resulting in a loss of coherence.

The CEvNS process can be represented by the reaction:

$$\nu(p) + \mathcal{N}(k) \rightarrow \nu(p') + \mathcal{N}(k') \quad (1)$$

where p, k are the incoming momenta of the neutrino and nucleus, respectively, and p', k' are the outgoing counterparts. The momentum transfer is then given by $t = (p - p')^2 = (k' - k)^2$. When evaluated in the lab frame (with the nucleus beginning at rest), this gives $t = -q^2 = -2m_T E_R$, where m_T and E_R are the mass and kinetic energy of the recoiling nucleus. With the mass of the neutrinos safely neglected, the maximum recoil an incoming neutrino of energy E_ν can impart is then

$$E_\nu^{\max} = \frac{2E_\nu^2}{m_T + 2E_\nu}. \quad (2)$$

The cross section is typically calculated by treating the nucleus as composed of point-like nucleons and accounting for their spatial extent within the nucleus via a form factor. This results in a standard form of the CEvNS cross section

$$\frac{d\sigma}{dE_R} = \frac{G_F^2 m_T}{4\pi} \left(1 - \frac{E_R m_T}{2E_\nu^2}\right) Q_w^2 F^2(q^2), \quad (3)$$

where $Q_w = Q_p Z + Q_n (A - Z)$ is the weak nuclear charge in terms of the proton and neutron weak charges and $F(q)$ is the nuclear form factor, typically taken to be of the Helm [20] or Klein-Nystrand [21] form.

The above is a good approximation to the CEvNS cross section, however, several improvements are variously made in the literature, which can have percent-level corrections. For example, in the above equation, the sub-leading kinematic factor E_R/E_ν , has been dropped. Additionally, one can take into account the different proton and neutron distributions within the nucleus, assigning them separate form factors [22]. Furthermore, while radiative corrections are typically included in the nucleon weak charges, there are additional flavor-dependent radiative corrections that can be included [23]. Lastly, some effort has been made to include the spin-dependent effects of the neutrinos coupling to odd- A nuclei [24, 25].

Putting these together, but neglecting the spin-dependent effects (which are small but will nevertheless be treated with more rigor in the following section) we can more accurately write the cross section as

$$\begin{aligned} \frac{d\sigma_{T\nu_i}}{dE_R} &= \frac{G_F^2 m_T}{4\pi} \left(1 - \frac{E_R m_T}{2E_\nu^2} - \frac{E_R}{E_\nu}\right) \\ &\times (Q_{p,\nu_i} F_p(q^2) + Q_n F_n(q^2))^2. \end{aligned} \quad (4)$$

Here the flavor dependent charges are taken from [23]:

$$\begin{aligned} Q_n &= -1.02352(25) \\ Q_{p,\nu_e} &= 0.0747(34), \quad Q_{p,\nu_\mu} = 0.0582(34). \end{aligned} \quad (5)$$

Using this equation requires knowledge of the proton and neutron distributions within the nucleus. While the former can be measured well due to its electric charge, the latter is not well constrained experimentally. Given the much larger weak charge of the neutron, the relatively unknown neutron form factor thus contributes the largest uncertainty to determinations of the CEvNS cross section.

III. NUCLEAR FORM FACTORS

Nuclear form factors are defined as the Fourier transform of density distributions of the nucleus:

$$F(q^2) = \int e^{i\vec{q}\cdot\vec{r}} \rho(r) d^3\vec{r}, \quad (6)$$

where $\rho(r)$ is the relevant density distribution, which is commonly assumed to be a spherically symmetric function. The root-mean-square (rms) radius for a density distribution is then given by

$$r_{\text{rms}}^2 \equiv \langle r^2 \rangle = \frac{\int \rho(r) r^2 d^3\vec{r}}{\int \rho(r) d^3\vec{r}}. \quad (7)$$

The density distribution used, i.e. electric charge-, weak charge- or mass-density, results in different form factors (and rms radii) which are appropriate for use in different scattering processes. Neutral-current neutrino scattering proceeds through the coupling of the Z-boson to the weak charge of the nucleus. Therefore CEvNS requires the use of weak-charge form factors which in turn require knowledge of the weak-charge density. We note that some past work has used experimentally determined electric-charge rms radii to construct form factors for CEvNS, but this can differ significantly from the weak-charge radii [26].

It is possible to measure the weak charge distribution through parity-violating electron scattering, which has been performed at Jefferson lab by the PREX and CREX experiments, on lead-208 and calcium-48 respectively. However, these experiments have only measured the weak charge at a single momentum transfer: $q = 0.76 \text{ fm}^{-1}$ and 1.28 fm^{-1} , respectively [27, 28]. Additionally, these experiments are difficult and unlikely to be performed on every isotope relevant to CEvNS. Therefore, it is necessary to use indirect knowledge of the weak-charge distribution from e.g. the electric charge distributions, or theoretical modelling.

In this work we will compare several methods for modelling the CEvNS form factors and determine their effect on the resulting cross sections. This includes theoretical

modelling using both Skyrme-Hartree-Fock (SHF) calculations and the nuclear shell model. The SHF results will allow us to accurately model the nucleon distributions, from which rms radii are computed. The shell model calculations will allow us to include sub-leading nuclear effects through the chiral EFT formalism of [15]. For comparison with previous work in the literature, we will also perform a data-driven calculation based on electric-charge radii.

When modelling the nucleus as a bound state of point-like nucleons, the neutron and proton point radius distributions $R_{n,p}$ are obtained from

$$R_n^2 = \frac{1}{A-Z} \int d^3r r^2 \rho_n(\mathbf{r}), \quad (8)$$

$$R_p^2 = \frac{1}{Z} \int d^3r r^2 \rho_p(\mathbf{r}), \quad (9)$$

respectively. Given that stable nuclei exhibit a common, almost uniform, saturating density it is possible to parameterise their density distributions (to very good accuracy) with fits to distributions of just two parameters: one which defines the size of the nucleus and another which defines the thickness of the ‘skin’ region at the surface. At low momentum transfers, the form factor remains relatively insensitive to differences in these parameterizations. To fit observation to a density distribution, it can be sufficient to equate a measured or theoretically determined rms radius with that of the parameterized distribution. We will make use of this matching process below.

A. From electric-charge densities

The most reliable access we have to the nuclear size and shape is via electromagnetic probes which couple to the electric charge distribution. Protons, being charged, contribute more to this distribution than the neutrons do. However, the reverse is true for the weak-charge distribution where neutrons dominate in their contribution. This makes the electric charge distribution an imperfect surrogate for the weak-charge distribution. To account for this difference, previous works have made some assumptions about the neutron distribution based on the proton distribution. In [22] the neutron rms radius was chosen to lie between the proton rms charge radius and an additional 0.3 fm. In [29], a fit is made to the proton-neutron radii difference data, however the large scatter in the data used in the fit tends to exaggerate the uncertainty for any one nucleus.

In this work we will follow the method of [22]. For our electric-charge inspired distributions we will use the Klein-Nystrand (KN) [21] model which has been previously used in CEvNS research (including by the COHERENT collaboration). The Klein-Nystrand form factor is based on both a Yukawa potential of range a_k and a hard

sphere distribution with radius r_A . It has the form

$$F_{\text{KN}}(q) = 3 \frac{\sin(qr_A) - qr_A \cos(qr_A)}{(qr_A)^3} [1 + (qa_k)^2]^{-1}, \quad (10)$$

where $a_k = 0.7$ fm and r_A is the nuclear radius. The nuclear radius is obtained by equating the rms radius for the distribution:

$$\langle r^2 \rangle_{\text{KN}} = \frac{3}{5} r_A^2 + 6a_k^2. \quad (11)$$

with the proton rms charge radius. The proton rms charge radii for the target nuclei $\sqrt{\langle r_p^2 \rangle} \equiv r_{\text{rms}}^p$ can be obtained from various experimental sources. The values we adopt are shown in Tab. I. The neutron rms radii are then taken to lie in the range $r_{\text{rms}}^n \leq r_{\text{rms}}^p \leq r_{\text{rms}}^n + 0.3$ fm for Ge, I and Cs, whilst for Ar the upper limit is taken to be $r_{\text{rms}}^p + 0.2$ fm. We use this range to bracket the uncertainty in the neutron distribution.

B. From Skyrme-Hartree-Fock distributions

To model the weak-charge distribution of the nucleus more accurately, we perform Skyrme-Hartree-Fock calculations to find the point-like nucleon distributions within the nucleus. While we have experimental probes of the electric-charge distributions, which dominantly probes the protons, for consistency we will also use the theoretical values for R_p in this calculation. The weak radius of the nucleus can then be calculated from:

$$R_W^2 = \frac{1}{Q_w} (ZQ_p(R_p^2 + r_{w,p}^2) + (A - Z)Q_n(R_n^2 + r_{w,n}^2)) \quad (12)$$

where $r_{w,p} = 1.545(17)$ fm and $r_{w,n} = 0.8434(12)$ fm are the weak radii of the proton and neutron, respectively.

The nucleon densities were evaluated with the SKYAX solver [31] assuming axial symmetry for several parametrizations of the Skyrme functional, namely SkM*, SLy6, SV-min and UNEDF1 as defined in SKYAX. Pairing correlations are treated at the BCS level with a ‘‘density-dependent delta interaction’’ (DDDI) for SV-min and SkM*, and with a ‘‘volume delta interaction’’ (VDI) for SLy6 and UNEDF1. The final theoretical values of $R_{p,n}$ are obtained from the average of the results for each interaction, while the standard deviations are used to evaluate the uncertainties. The full results for each interaction are compiled in the appendix (Table VI). From this we find the average and standard deviation for each isotope and use it to compute weak radii from Eq. (12). The results are summarised in Table II.

For simplicity we then parameterize the distribution via the symmetrized 2-parameter Fermi (Fermi) model [32], which has been shown to provide a reasonable fit to similar calculations [26]. The Fermi distribution is defined by:

$$\rho(r) = \rho_0 \frac{\sinh(c/a)}{\cosh(r/a) + \cosh(c/a)}, \quad (13)$$

where its two parameters c and a relate to the size and thickness of the skin, respectively. The rms radius of this distribution is:

$$\langle r^2 \rangle = \frac{3}{5} c^2 + \frac{7}{5} \pi^2 a^2, \quad (14)$$

and the normalization constant is

$$\rho_0 = \frac{3Q_w}{4\pi c(c^2 + \pi^2 a^2)}. \quad (15)$$

The (normalised) form factor is then:

$$F_F(q) = \frac{3}{qc} \left(\frac{\sin(qc)}{(qc)^2} \frac{\pi qa}{\tanh(\pi qa)} - \frac{\cos(qc)}{qc} \right) \times \frac{\pi qa}{\sinh(\pi qa)} \frac{1}{1 + (\pi a/c)^2} \quad (16)$$

Motivated by the results for the weak skin of calcium and lead in [26], in this work we set $a = 0.55 \pm 0.05$ fm. We then derive the parameter c by equating $R_W = \langle r^2 \rangle$, i.e. Eq. (14) with Eq. (12).

IV. DETAILED NUCLEAR TREATMENT

The formalism discussed thus far has been derived top-down, dealing with the most dominant contributions of neutrino-nucleus couplings. However, this does not systematically account for the nuclear effects stemming from the neutrino coupling to both vector (spin-independent) and axial-vector (spin-dependent) currents within the nucleus. These effects are generally expected to be small and therefore are typically ignored.

The full, bottom-up, calculation starts with the hadronic currents within the nucleus and using effective field theory, derives the Wilson coefficients for the nuclear couplings. This task has been performed for the CEvNS process, in full generality, in [15]. The resulting cross section is much like the traditional form of Eq.(3), with an additional term for the axial form factor:

$$\frac{d\sigma_A}{dE_R} = \frac{G_F^2 m_T}{4\pi} \left(1 - \frac{m_T E_R}{2E_\nu^2} - \frac{E_R}{E_\nu} \right) Q_w^2 |F_w(\mathbf{q}^2)|^2 + \frac{G_F^2 m_T}{4\pi} \left(1 + \frac{m_T E_R}{2E_\nu^2} - \frac{E_R}{E_\nu} \right) F_A(\mathbf{q}^2), \quad (17)$$

However, the full form of the nuclear form factors go beyond the density distributions discussed previously. The Weak form factor takes the form

TABLE I: Experimental charge rms radii r_{rms}^p values (in fm) for ^{40}Ar , $^{70,72,73,74,76}\text{Ge}$, ^{127}I and ^{133}Cs , obtained from [30].

	^{40}Ar	Ge					^{127}I	^{133}Cs
		70	72	73	74	76		
r_{rms}^p	3.4274(26)	4.0414(12)	4.0576(13)	4.0632(14)	4.0742(12)	4.0811(12)	4.7500(81)	4.8041(46)

TABLE II: Skyrme-Hartree-Fock predictions of rms point-like proton and neutron radii and the resulting predicted RMS Weak radius.

Nucleus	R_p (fm)	R_n (fm)	R_W (fm)
^{40}Ar	3.326(25)	3.420(17)	3.514(17)
^{70}Ge	3.930(21)	3.986(12)	4.065(12)
^{72}Ge	3.946(20)	4.036(12)	4.116(12)
^{73}Ge	3.954(19)	4.059(11)	4.140(12)
^{74}Ge	3.963(18)	4.084(10)	4.165(11)
^{76}Ge	3.993(20)	4.143(14)	4.224(15)
^{127}I	4.688(14)	4.824(9)	4.895(10)
^{133}Cs	4.750(12)	4.887(8)	4.957(9)

$$\begin{aligned}
F_w(\mathbf{q}^2) = & \frac{1}{Q_w} \left[\left(Q_w^p \left(1 + \frac{\langle r_E^2 \rangle^p}{6} t + \frac{1}{8m_N^2} t \right) \right. \right. \\
& + Q_w^n \frac{\langle r_E^2 \rangle^n + \langle r_{E,s}^2 \rangle^N}{6} t \left. \right) \mathcal{F}_p^M(\mathbf{q}^2) \\
& + \left(Q_w^n \left(1 + \frac{\langle r_E^2 \rangle^p + \langle r_{E,s}^2 \rangle^N}{6} t + \frac{1}{8m_N^2} t \right) \right. \\
& + Q_w^p \frac{\langle r_E^2 \rangle^n}{6} t \left. \right) \mathcal{F}_n^M(\mathbf{q}^2) \\
& - \frac{Q_w^p (1 + 2\kappa^p) + 2Q_w^n (\kappa^n + \kappa_s^N)}{4m_N^2} t \mathcal{F}_p^{\Phi''}(\mathbf{q}^2) \\
& \left. - \frac{Q_w^n (1 + 2\kappa^p + 2\kappa_s^N) + 2Q_w^p \kappa^n}{4m_N^2} t \mathcal{F}_n^{\Phi''}(\mathbf{q}^2) \right], \quad (18)
\end{aligned}$$

where m_N is the nucleon mass and the remaining constants are provided in [15]. The weak form factor hence depends on the coherent and semi-coherent responses F_N^M and $F_N^{\Phi''}$, respectively, where $N = \{p, n\}$ denotes protons and neutrons. The axial-vector form factor has the form

$$\begin{aligned}
F_A(\mathbf{q}^2) = & \frac{8\pi}{2J+1} \\
& \times \left((g_A^{s,N})^2 S_{00}^T(\mathbf{q}^2) - g_A g_A^{s,N} S_{01}^T(\mathbf{q}^2) + (g_A)^2 S_{11}^T(\mathbf{q}^2) \right) \quad (19)
\end{aligned}$$

where, in the isospin-basis, we have the spin structure functions in terms of the nuclear responses $\mathcal{F}_{\pm}^{\Sigma'L} = \mathcal{F}_p^{\Sigma'L} \pm \mathcal{F}_n^{\Sigma'L}$:

$$\begin{aligned}
S_{00}^T &= \sum_L \left[\mathcal{F}_+^{\Sigma'L}(\mathbf{q}^2) \right]^2, \\
S_{11}^T &= \sum_L \left[[1 + \delta'(\mathbf{q}^2)] \mathcal{F}_-^{\Sigma'L}(\mathbf{q}^2) \right]^2, \quad (20) \\
S_{01}^T &= \sum_L 2 [1 + \delta'(\mathbf{q}^2)] \mathcal{F}_+^{\Sigma'L}(\mathbf{q}^2) \mathcal{F}_-^{\Sigma'L}(\mathbf{q}^2),
\end{aligned}$$

The correction to the leading SD coupling for the transverse SD response $\delta'(\mathbf{q}^2)$ is given in [15]. In this more-detailed treatment of the nucleus, the full Weak radius receives additional contributions from spin-orbit effects and the strange electric-charge distribution. It takes the form

$$\begin{aligned}
R_w^2 = & \frac{ZQ_w^p}{Q_w} \left(R_p^2 + \langle r_E^2 \rangle^p + \frac{Q_w^n}{Q_w^p} (\langle r_E^2 \rangle^n + \langle r_{E,s}^2 \rangle^N) \right) \\
& + \frac{NQ_w^n}{Q_w} \left(R_n^2 + \langle r_E^2 \rangle^p + \langle r_{E,s}^2 \rangle^N + \frac{Q_w^p}{Q_w^n} \langle r_E^2 \rangle^n \right) \\
& + \frac{3}{4m_N^2} + \langle \tilde{r}^2 \rangle_{\text{so}}, \quad (21)
\end{aligned}$$

where the spin-orbit contribution is given by:

$$\begin{aligned}
\langle \tilde{r}^2 \rangle_{\text{so}} = & - \frac{3Q_w^p}{2m_N^2 Q_w} \left(1 + 2\kappa^p + 2 \frac{Q_w^n}{Q_w^p} (\kappa^n + \kappa_s^N) \right) \mathcal{F}_p^{\Phi''}(0) \\
& - \frac{3Q_w^n}{2m_N^2 Q_w} \left(1 + 2\kappa^p + 2\kappa_s^N + 2 \frac{Q_w^p}{Q_w^n} \kappa^n \right) \mathcal{F}_n^{\Phi''}(0). \quad (22)
\end{aligned}$$

To apply this formalism and calculate cross sections for a given target we will employ the nuclear shell model to compute the nuclear responses above.

A. Evaluating the nuclear responses

To compute the weak and axial-vector nuclear form factors in Eqs. (18) and (19), we need to evaluate the \mathcal{F}_N^M , $\mathcal{F}_N^{\Phi''}$ and $\mathcal{F}_N^{\Sigma'L}$ nuclear responses. The nuclear responses originate from a multipole decomposition of the lepton-nucleus amplitude, developed in [33, 34]. Here, they are defined as:

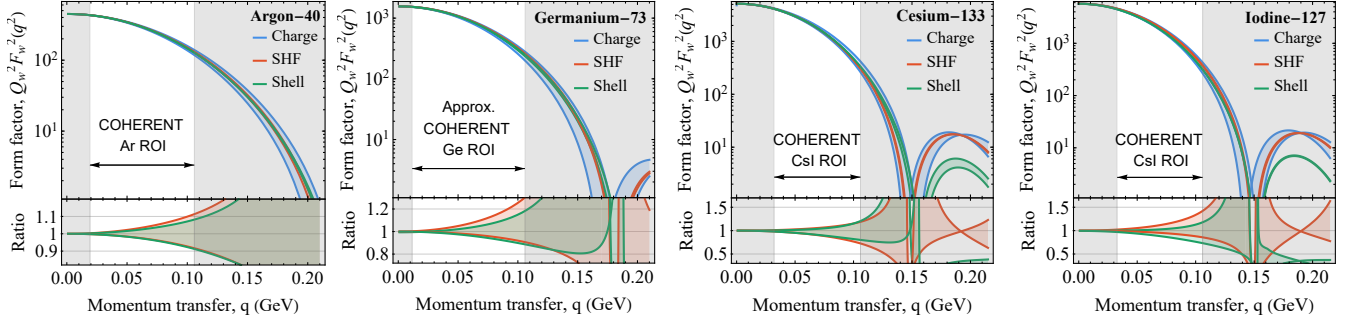


FIG. 2: Spin-independent weak form factors for CEvNS in the four targets relevant to current experiments. Bands show the error due to uncertainties in the neutron distribution (Charge) and from using different interactions (SHF and Shell model).

$$\begin{aligned}
 |\mathcal{F}_N^X(q^2)|^2 &\equiv \frac{4\pi}{2J_i+1} \sum_{J=0} \langle J_i || X_J^{(N)} || J_i \rangle \langle J_i || X_J^{(N)} || J_i \rangle, \\
 |\mathcal{F}_N^{\Sigma'}(q^2)|^2 &\equiv \sum_{J=1} \langle J_i || \Sigma_J^{(N)} || J_i \rangle \langle J_i || \Sigma_J^{(N)} || J_i \rangle,
 \end{aligned}
 \tag{23}$$

where J_i is the nuclear ground state angular momentum, and the nuclear operators $X = M$, Φ'' and Σ' are given in Appendix C.

The nature of these operators can be understood from their long-wavelength ($q \rightarrow 0$) limit (provided in Table III). The M operator is spin-independent (SI) and adds coherently from all nucleons, giving rise to the standard coherent enhancement of CEvNS. The Φ'' term in the $q \rightarrow 0$ limit is proportional to a spin-orbit operator, and is sensitive to nucleon occupations of the spin-orbit partner levels. This partially coherent operator is highest when one spin-orbit partner is filled and the other is empty. The Σ' operator is spin-dependent (SD), picking out the transverse projection of the spin current. All nuclei have non-zero responses to the M and Φ'' operators, while only odd-nuclei with a $J_i \neq 0$ ground state have a Σ' response.

Using the Wigner-Eckhart theorem the nuclear matrix elements in Eq. (23) can be reduced in angular momentum and isospin:

$$\begin{aligned}
 \langle J_i; TM_T || \sum_{m=1}^A \hat{O}_{J,\tau}(q\vec{x}_m) || J_i; TM_T \rangle &= (-1)^{T-M_T} \\
 \begin{pmatrix} T & \tau & T \\ -M_T & 0 & M_T \end{pmatrix} \langle J_i; T :: \sum_{m=1}^A \hat{O}_{J,\tau}(q\vec{x}_m) :: J_i; T \rangle.
 \end{aligned}
 \tag{24}$$

Here, $\hat{O}_{J,\tau}$ signify the nuclear operators, with $\hat{O}_{J,\tau} = \hat{O}_J \tau_3^\tau$ and τ_3 being the nucleon isospin operator ($\tau = \{0, 1\}$). The isospin-independent(dependent) component is given by the $\tau = 0$ ($\tau = 1$) term.

This can then be written as a product of single-nucleon matrix elements and one-body density matrix elements

$$\begin{aligned}
 (\text{OBDMEs}) \Psi_{|\alpha|,|\beta|}^{J;\tau} &\text{ in the harmonic oscillator basis [36]:} \\
 \langle J_i; TM_T || \sum_{m=1}^A \hat{O}_{J,\tau}(q\vec{x}_m) || J_i; TM_T \rangle &= (-1)^{T-M_T} \\
 \times \begin{pmatrix} T & \tau & T \\ -M_T & 0 & M_T \end{pmatrix} \sum_{|\alpha|,|\beta|} \Psi_{|\alpha|,|\beta|}^{J;\tau} \langle |\alpha| :: \hat{O}_{J,\tau}(q\vec{x}) :: |\beta| \rangle.
 \end{aligned}
 \tag{25}$$

These OBDMEs hold all the nuclear structure information for any nucleus of interest, and can be calculated using the nuclear shell model. The harmonic-oscillator states for single nucleons, α and β , are defined by the quantum numbers $\beta = \{n_\beta, l_\beta, j_\beta, m_{j_\beta}, m_{t_\beta}\}$, with the reduced state notation $|\beta| = \{n_\beta, l_\beta, j_\beta\}$. The nucleon isospin state $t_\beta = t_\alpha = 1/2$ is implicit in the notation. The nuclear isospin is denoted by T and its projection

M_T . The notation $::$ denotes a matrix element reduced in both angular momentum and isospin. The explicit form of the reduced matrix elements is given in Appendix C. The OBDMEs have the form

$$\Psi_{|\alpha|,|\beta|}^{J;\tau} \equiv \frac{\langle J_i; T :: [a_{|\alpha|}^\dagger \otimes \tilde{a}_{|\beta|}]_{J;\tau} :: J_i; T \rangle}{\sqrt{(2J+1)(2\tau+1)}},
 \tag{26}$$

where $\tilde{a}_\beta = (-1)^{j_\beta - m_{j_\beta} + 1/2 - m_{t_\beta}} a_{|\beta|; -m_{j_\beta}, -m_{t_\beta}}$ and \otimes denotes a tensor product. This basis gives response functions of the form $e^{-2y} p(y)$, where $p(y)$ is a polynomial with $y = (qb/2)^2$ and $b = 1/\sqrt{m_N \omega} \approx \sqrt{41.467/(45A^{-1/3} - 25A^{-2/3})}$ fm is the harmonic oscillator length parameter (ω is the oscillator frequency).

B. Form factors from shell model calculations

Large-scale nuclear shell model calculations were performed using NuShellX [37], which is often employed to obtain theoretical energies, wave functions and spectroscopic overplots for a wide range of nuclei. The program's

TABLE III: Leading order terms of the nuclear operators in the long-wavelength limit $q \rightarrow 0$ [35].

Response Type	Leading Multipole	Long-wavelength Limit
M_{JM} : Charge	$M_{00}(q\vec{x}_m)$	$\frac{1}{\sqrt{4\pi}}1(m)$
T_{JM}^{el5} : Axial Transverse Electric	$\Sigma'_{1M}(q\vec{x}_m)$	$\frac{1}{\sqrt{6\pi}}\sigma_{1M}(m)$
L_{JM} : Longitudinal	$\frac{q}{m_N}\Phi''_{00}(q\vec{x}_m)$	$-\frac{q}{3m_N\sqrt{4\pi}}\vec{\sigma}(m)\cdot\vec{l}(m)$
	$\frac{q}{m_N}\Phi''_{2M}(q\vec{x}_m)$	$-\frac{q}{m_N}\frac{1}{\sqrt{30\pi}}\left[x_m \otimes \left(\vec{\sigma}(m) \times \frac{\vec{\sigma}}{i}\right)_1\right]_{2M}$

inputs include the relevant valence space for the nucleus/isotope of interest - which constitutes a set of single nucleon levels above a completely filled nuclear core - as well as its corresponding list of two-body interactions. Each interaction is fitted to a set of experimental nuclear data for a range of nuclei in the relevant valence space. The contemporary approach is to derive the interactions from the nucleon-nucleon interaction using effective field theory. The interactions are then fine tuned by fitting a limited number of parameters to a body of nuclear data - usually excitation energies in a range of nuclei in the valence space. The aforementioned OBDMEs are extracted for the valence space levels, with the values dependent on the particular shell model interactions used.

In this work we explore a variety of shell model interactions and truncations for our chosen targets: ^{40}Ar , $^{70,72,73,74,76}\text{Ge}$, ^{127}I , and ^{133}Cs . Using the shell model calculations detailed below, we extract the OBDME for all targets. The OBDMEs are then used to compute the nuclear responses using the Mathematica package described in [38]. Analytic form factor expressions for ^{40}Ar , $^{70,72,73,74,76}\text{Ge}$ and ^{127}I are provided in [39], while those for ^{133}Cs are provided in Appendix D 8. The form factors for each of the nuclear responses M , Φ'' and Σ' are plotted as functions of q in Appendix D. The form factors are used to derive point-proton, point-neutron and weak radii for all isotopes for comparison with those obtained with our SHF calculations, and are given in Table VII of Appendix A. Additionally, we make comparisons with experimental energy spectra, moments and transitions in Appendix B.

The shell-model derived Weak form factors are shown in Fig. 2, compared to form factors based on the charge distribution and SHF calculations. The uncertainty band denotes the range of values obtained given the different shell model interactions. The shell model results for each isotope show good agreement with each other (low overall uncertainty) and fall within the large uncertainty band of the form factors derived from the charge distribution. They are also generally in very good agreement with the SHF results within the experimentally accessible regions of interest. The axial form factor is shown in Fig. 3 for each interaction individually.

The sections below outline the valence space, valence space truncation and shell model interactions used in this work for each target.

^{40}Ar

The *sdpf* valence space was employed for this nucleus, which constitutes single particle levels $1d_{5/2}$, $2s_{1/2}$, $1d_{3/2}$, $1f_{7/2}$, $2p_{3/2}$, $1f_{5/2}$ and $2p_{1/2}$. The valence space truncation employed consisted of an unrestricted *sd* shell and an empty *pf* shell for the protons, and a full *sd* shell with an unrestricted *pf* shell for the neutrons. Four shell model interactions were used, namely SDPF-NR [40], SDPF-U [41], EPQQM [42] and SDPF-MU [43], all of which consider a ^{16}O core. This isotope was not considered in the work of [35, 38].

The ^{40}Ar theoretical energy levels for the above shell model interactions are plotted against the experimental values in Fig. 5. The first two theoretical energy levels for all interactions are consistent with experiment within ~ 200 keV, except for SDPF-MU which is within ~ 400 keV from experiment for the 2_1^+ state. Overall, the energy spectrum of the EPQQM interaction is least consistent with the other shell model calculations and with experiment, with the spectrum being much more sparse and spread out in the level spacings.

The magnetic dipole and electric quadrupole moments and transitions are presented in Table VIII, where the effective g factors and charges employed take on values of $e_p = 1.5$, $e_n = 0.5$, $g_{sp} = 5.586$, $g_{sn} = -3.826$, $g_{lp} = 1$, and $g_{ln} = 0$. Information on the ground state is most important for comparison with theoretical values, as it is used in the scattering calculations here. However, as the ground state of ^{40}Ar is 0^+ , the magnetic dipole and electric quadrupole moment values are identically zero. Nevertheless, we employ the next non-zero state (2_1^+), which can give an indication of the overall accuracy of the calculation through information on the spectrum beyond the ground state. It is found that the shell model moments are not consistent with experimental values, and most experimental transitions are poorly reproduced as well.

The reason for the failure of the shell model for the case of ^{40}Ar is understood: the assumption that ^{40}Ca is an inert core is not justified. Its ground state is near spherical, as assumed in the shell model, but it has low-excitation deformed states formed by exciting pairs of protons and neutrons across the shell gaps at $N = 20$ and $Z = 20$. This leads to mixing between the spherical shell model states and the deformed states in nuclei like ^{40}Ar . The case of ^{42}Ca , an isotone of ^{40}Ar , is best studied, as has recently been reviewed by Stuchbery and

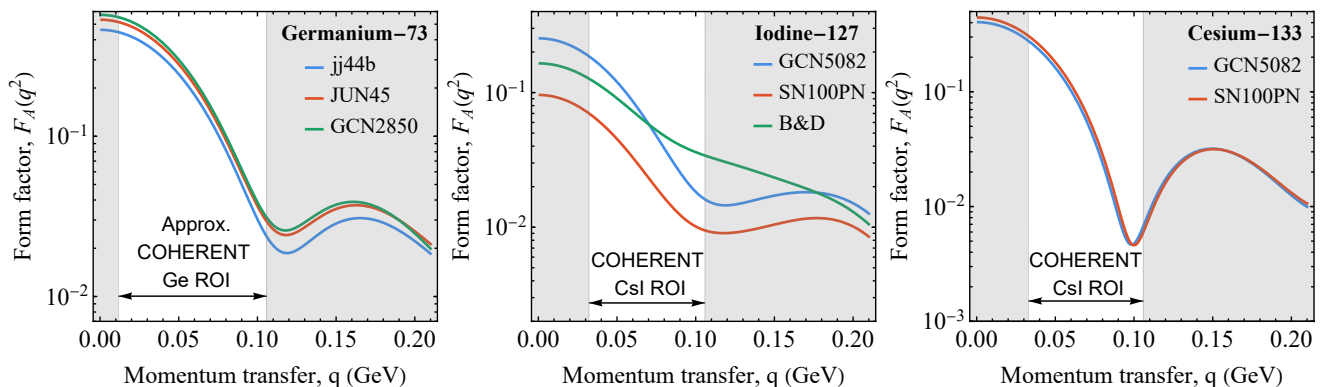


FIG. 3: Spin-dependent form factors relevant to CEvNS for the three $J_i \neq 0$ targets we consider. The curves denote the different shell model interactions as described in the text.

Wood [44]. They infer that the first 2^+ state of ^{42}Ca is about 50% due to the spherical shell model configuration. The ground state is about 65% of the shell model configuration. Similar mixing is present in ^{40}Ar . Thus the shell model calculations performed here are limited by the presence of configuration mixing well beyond the usual valence space.

The obtained form factors are compared against those based on the SHF calculations and the charge distribution in Appendix D. The maximum difference between the form factors for the M response at the minimum q value is $\sim 0.3\%$, and $\sim 11\%$ at the maximum q value. For Φ'' , these values are $\sim 24\%$ and $\sim 21\%$, respectively, where the largest differences occur between the SDPF-MU and EPQQM interactions.

$^{70,72,73,74,76}\text{Ge}$

The germanium shell model calculations were performed in the $f_5p_9g_9$ model space, which consists of the single-particle levels $2p_{3/2}$, $1f_{5/2}$, $2p_{1/2}$ and $1g_{9/2}$. The work of [35, 38] employed the GCN2850 interaction [45], with a valence space truncation that consisted of limiting the occupation number of the $1g_{9/2}$ level to no more than two nucleons above the minimum occupation for all isotopes. Here, we consider an unrestricted $f_5p_9g_9$ model space with the JUN45 [46] and jj44b [47] interactions.

The experimental energy spectra are plotted against the theoretical shell model ones for the even isotopes in Fig. 6 (Appendix B 2). The spectra comparison for ^{73}Ge is provided in [39], alongside a brief summary of the two aforementioned shell model interactions, where the theoretical spectra were found to be inconsistent with another, and not particularly consistent with experiment. In the cases of $^{70,72,74}\text{Ge}$, the low-lying experimental spectra are a little better reproduced by the JUN45 interaction results, which was fitted to the Ge isotopes in consideration (the jj44b interaction on the other hand was not fitted to these). The shell model spectra for ^{76}Ge are practically identical to one another up to ~ 1.9 MeV.

An agreement between theoretical and experimental levels of ~ 200 keV would be considered satisfactory for such shell model calculations using heavier nuclei, however this agreement exists only for some levels of the even isotopes.

The experimental and theoretical magnetic dipole and electric quadrupole moments and transitions are provided for the even isotopes in Tables IX and X. Much like with ^{40}Ar , the magnetic and electric moment information is not available for the ground state 0^+ , however the subsequent non-zero states are used here as a test of the overall accuracy of the shell model code. As before, the values for ^{73}Ge are provided in [39]. For the magnetic dipole moments of the even isotopes, the experimental 2^+_1 and 4^+_1 states are well reproduced by both shell model interactions, whereas the jj44b value of the 2^+_2 state is consistently closer to experiment compared to JUN45. The 2^+_1 electric quadrupole moment is quite inconsistent with the experimental values for $^{70,72,74}\text{Ge}$, where only the jj44b ^{76}Ge value lies within the experimental range.

The individual germanium form factors are plotted (for the M , Φ'' and Σ' responses) in Appendix D, and compared against the SHF and charge distribution form factors. The M response is consistent amongst all calculations, with a maximum difference of $\sim 0.2\%$ at the lower end of the COHERENT q region-of-interest (ROI) for the even isotopes, and $\sim 3\%$ at the higher end for $^{70,72}\text{Ge}$. For ^{73}Ge these take on the values of $\sim 0.3\%$, and $\sim 20\%$ at the higher end for $^{73,74,76}\text{Ge}$. For the Φ'' channel, the maximum difference is observed between the GCN2850 and jj44b shell model calculations, which is $\sim 80\%$ for ^{70}Ge at both ends of the q spectrum, factor of ~ 2.4 for ^{72}Ge , factor of ~ 2.3 for ^{73}Ge , factor of ~ 2.2 for ^{74}Ge , and $\sim 60\%$ for ^{76}Ge . The difference in the SD Σ' channel for ^{73}Ge is $\sim 30\%$ at both ends of the q ROI.

^{127}I

The iodine calculations were performed in the model space which includes all proton and neutron orbits in the major shell between magic numbers 50 and 82, with single particle levels $1g_{7/2}$, $2d_{5/2}$, $2d_{3/2}$, $3s_{1/2}$ and $1h_{11/2}$. The work of [35, 38] utilises a nuclear shell model interaction developed by Baldridge and Dalton [48], which we refer to as “B&D” [39]. The valence space restriction employed in [35, 38] involves fixing the occupation number of $1h_{11/2}$ to the minimum allowed nucleon number.

Here, we consider the SN100PN [49] and GCN5082 [45] interactions, and perform two calculations for each. Our shell model calculations are performed in the same model space as the B&D calculations of [35, 38], but with different restrictions. The model space restrictions employed in our work are the same as those in [39], with the four different calculations given the names “SN100PN” and “GCN5082” (which share the same truncation), as well as “Truncated SN100PN” (with a more truncated scheme), and “GCN5082 Expanded” (with an alternative truncation to “GCN5082”). The theoretical energy spectra are plotted against the experimental ones in [39], in addition to the theoretical and experimental electric quadrupole and magnetic dipole moments, with the proton and neutron effective charges and g factors also provided in [39].

The M , Φ'' and Σ' form factors for the above calculations are compared against the SHF and charge distribution form factors in Appendix D. The maximum difference between the form factors for the M channel at the minimum q value is $\sim 1\%$, and $\sim 30\%$ at the maximum q value. For Φ'' , these values are $\sim 55\%$ and $\sim 50\%$, respectively. For Σ' , the factor differences are ~ 44 and ~ 81 , due to the large difference between the Truncated SN100PN calculation and the remaining calculations. This is consistent with the integrated form factor (IFF) results in [39], which showed a more pronounced difference between the SD Truncated SN100PN IFF results and other calculations. This indicates that a more severe valence space truncation for a shell model interaction has a larger effect compared to a second more comparable truncation.

 ^{133}Cs

Here, we consider the same valence space and shell model interactions (SN100PN and GCN5082) as ^{127}I above. We have performed four calculations for ^{133}Cs , two of which employ the same truncations as the “SN100PN” and “GCN5082” calculations in Section IV B (and are given the same names here). We consider two additional calculations, one each for the SN100PN and GCN5082 interactions, where the neutron $2d_{5/2}$ level now has a minimum of 4 neutrons (as opposed to previously being completely filled), with the remainder of the proton and neutrons levels retaining the previous truncations. This is to explore the effect of a less truncated valence

space on the final results. These two additional calculations are termed “SN100PN Expanded” and “GCN5082 Expanded”.

The experimental energy spectra are plotted against the theoretical values for all the above calculations in Fig. 7. Only the SN100PN result reproduces the correct ground state spin and parity of $7/2^+$, however all four calculations reproduce the correct spins and parities of the three lowest-lying states within 200 keV of experiment. For both shell model interactions, using a less truncated valence space causes the spacing of the levels to widen compared to the original calculations, generally pushing the spectrum further up. This is likely due to the opening up of the $2d_{5/2}$ level in these calculations.

The experimental and theoretical magnetic dipole and electric quadrupole moments and transitions are provided in Tables XI and XII. The proton and neutron effective charges and g factors employed here are the same as those used in [39] for ^{127}I . The experimental magnetic dipole moments are much better reproduced by the shell model calculations compared to the electric quadrupole ones. The experimental electric quadrupole transitions are only reproduced within the uncertainty margins by the GCN5082 calculation, specifically for transitions from the $5/2_1^+$ and $3/2_1^+$ states to the ground state. On the other hand, the theoretical magnetic dipole transition values are not consistent with experiment. However, the important test of the shell model wavefunction is the magnetic dipole moment, which is sensitive to the wavefunction of the single state, and to the single nucleon structure of the state, rather than to emerging collective properties, which affect the E2 transition rates and the quadrupole moments. The magnetic dipole transitions are suppressed among the dominant low-excitation configurations, as is evident from their small values, and so become very sensitive to small component in the wavefunction that are not of interest here. Despite the lack of agreement for some observables, the present shell model calculations can be trusted to include the important single-particle configurations in the ground-state wavefunction.

The M , Φ'' and Σ' form factors for the above calculations are compared against the SHF and KN ones in Appendix D. The maximum difference between the form factors for the M channel at the minimum q value is $\sim 1\%$, and $\sim 20\%$ at the maximum q value. For Φ'' , these values are $\sim 6\%$ and $\sim 7\%$, respectively. For Σ' , these differences are $\sim 13\%$ and $\sim 18\%$.

TABLE IV: Our CEvNS cross section predictions in units of 10^{-40}cm^2

Target	Charge	SHF	Shell Mod.	COHERENT	
				Prediction	Exp.
Ar	18.65(22)	18.68(6)	18.64(5)	18.0(4)	23(7)
Ge	59(1)	59.8(2)	59.2(2)	-	-
CsI	189(4)	189.3(5)	186.3(5)	189(6)	165(30)

V. EXPERIMENTAL OBSERVABLES

To date, CEvNS has been observed by the COHERENT collaboration using the stopped pion source of neutrinos from the SNS, with both cesium-iodide [50] and argon [2] detector targets. Presently COHERENT have also deployed a germanium detector and measurements are ongoing. There are also experiments aiming to measure CEvNS from reactor neutrinos, including CONUS [51], RICOCHET [52] and NUCLEUS [53]. However, the momentum transfer from reactor neutrinos is very small and thus the form factor has little effect on the cross section. We therefore choose to focus our present analysis on the cesium-iodide, argon and germanium targets of COHERENT and leave reactor based experiments to a future work.

A. Flux averaged cross sections

First we calculate the flux averaged cross sections, by performing a weighted average of the cross sections over the three incoming neutrino flavor spectra and the isotopes in the target:

$$\langle\sigma\rangle_{\Phi} = \int dE_{\nu} \frac{d\phi}{dE_{\nu}} \int dE_R \frac{d\sigma}{dE_R}. \quad (27)$$

Here the neutrino spectra, $\frac{d\phi}{dE_{\nu}}$, are normalized to unity. For this calculation we use the neutrino spectra provided in [54], which were derived from detailed GEANT4 simulations of the proton beam colliding in the mercury spallation target. The uncertainties in the cross sections are determined from two sources: the form factors and the nucleon charges. We neglect uncertainties in the modelling of the neutrino spectra, which are unavailable, but note that errors in the spectra should affect all of the compared cross sections approximately the same. The form factor uncertainties are found by computing the flux averaged cross section with our two extremal form factors for each model (i.e. the upper and lower limits of the bands shown in Fig. 2). The central value and uncertainty is then taken as $(\sigma_{\max} + \sigma_{\min})/2$ and $(\sigma_{\max} - \sigma_{\min})/2$, respectively. The uncertainty in the nucleon charges is taken from [23]. The total uncertainty is determined by summing these two sources in quadrature. The KN and SHF models are calculated using Eq. (4), while the shell model result uses the full cross section in Eq. (3). The results of this calculation are shown in Fig. 1 and provided numerically in table IV.

Our argon results are all in very close agreement with each other, owing to the fact that argon is an even-even nucleus which doesn't receive large spin-orbit, and no spin-dependent, contributions. This result is slightly larger than the COHERENT prediction, though with the large uncertainties, is still in reasonable agreement. Our detailed nuclear results do shrink the uncertainty band, though it will be some time before the statistical errors in the experimental results make this difference relevant.

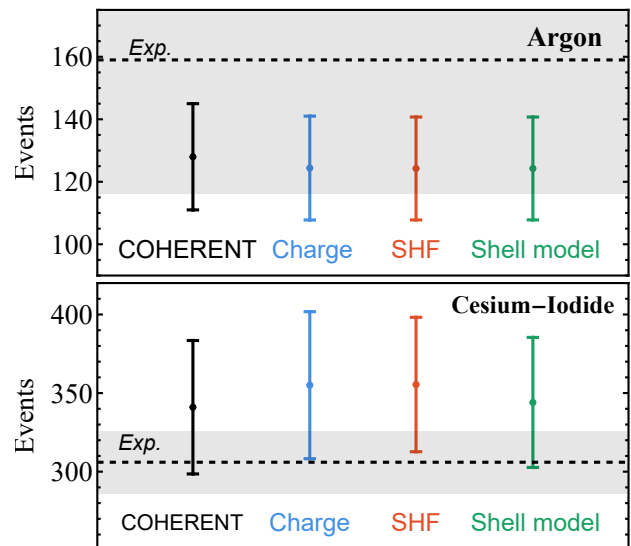


FIG. 4: Total event count predictions for the COHERENT experiment's argon and cesium-iodide detectors, using our 3 cross section calculations. Also shown is COHERENT's theoretical prediction and experimental result.

Our cesium-iodide results are in good agreement with the COHERENT prediction. Here we do see a small difference between our shell model results and the SHF calculations. While both cesium and iodine are odd nuclei, the axial term is a positive contribution and so the resulting difference stems from the spin-orbit term.

Our germanium results show a similar trend to the cesium-iodide results, with the shell model results being slightly smaller than the SHF results, which are both with the prior uncertainty derived from charge distributions. Presently there are no COHERENT results to compare with, though they are expected in the near future.

Fig. 1 also shows what a potential future experiment may measure with a combined error of 5%. We chose this level of error as it should be attainable in the coming years with additional statistics and ongoing measurements of the SNS flux with a D₂O detector, which are expected to reduce flux uncertainties to below 5%. For presentation purposes we have assumed the same mean $\langle\sigma\rangle_{\Phi}$ and simply shrunk the errors. This highlights the importance of our results for increasing the sensitivity of COHERENT to potential new-physics signals. Taking CsI as an example, if such a precise experimental measurement were made (i.e. $\langle\sigma\rangle_{\Phi} = (165 \pm 8) \times 10^{-40}$ cm²), the existing predictions would be merely in 2σ tension with this result, while our prediction would be well in tension at greater than 5σ .

We note that the assumed cross section model will affect the experimentally determined flux averaged cross section through the calculation of the experiment's sensitivity. Thus as measurements become better, one must be cautious to not interpret deviations of experimental

results from predictions which used a different cross section model. For a direct comparison with the observable experimental results we also compute the predicted number of events for COHERENT's detectors.

B. Experimental event counts

The differential scattering rate of neutrinos from nuclei, per target and incoming neutrino, is found by integrating over the incoming neutrino spectra and summing them:

$$\frac{dR}{dE_R} = \sum_i \int_{E_\nu^{\min}} dE_\nu \frac{d\phi}{dE_\nu} \frac{d\sigma_{T\nu_i}}{dE_R}. \quad (28)$$

Here, the neutrino flux is integrated from the minimum neutrino energy that can induce a recoil of energy E_R :

$$E_\nu^{\min} = \sqrt{\frac{E_R m_T}{2}}. \quad (29)$$

To go from the raw scattering rate to the expected number of counts in an experiment we follow the recipes provided by the COHERENT collaboration in [54] and [55]. The total number of detected CEvNS events is found by integrating over the detected energy taking into account the quenching of nuclear recoils, detector resolution effects and the energy dependent detection efficiency. For the cesium-iodide detector this has the form

$$N_{\text{events}}^{\text{CsI}} = N_T \Phi \int dPE \epsilon(PE) \times \int dE_R P(PE|E_R) \frac{dR}{dE_\nu}, \quad (30)$$

while for the argon detector the form is

$$N_{\text{events}}^{\text{Ar}} = N_T \Phi \int dE_{ee} \epsilon(E_{ee}) \times \int dE_R P(E_{ee}|E_R) \frac{dR}{dE_\nu}, \quad (31)$$

where PE is the detected photoelectrons, N_T is the number of targets in the detector and $\Phi = \frac{\text{POT} f_\pi}{4\pi d^2}$ is total number of neutrinos (per flavor) expected at the target [calculated from the total number of protons on target (POT) and the average number of pions produced per POT, f_π]. The values for the experimental parameters are summarized in table V.

TABLE V: Parameters for the COHERENT experimental runs that we considered in this work

Target	Mass	Distance	POT	$\langle \pi/\text{POT} \rangle$
argon	24.4 kg	27.5 m	1.38×10^{23}	0.09
cesium-iodide	14.6 kg	19.3 m	3.20×10^{23}	0.0848

The resulting expected counts for the two detectors' runs are shown in Fig. 4. The uncertainty in the number of counts is determined from two sources: the uncertainty in the cross section (calculated as above), and from

the experimental systematic uncertainty (which is dominated by the 10% uncertainty in the total neutrino flux). We take our systematic uncertainty from COHERENT's analysis (not including their theoretical uncertainties): 13% for argon and 12% for cesium iodide.

Overall we achieved good agreement reproducing COHERENT's results, with all predictions well within the errors for both COHERENT's predictions and experimental results. However, without knowledge of their exact theoretical model it is difficult to reproduce the result precisely. In this instance the result obtained using the form factor derived from the electric-charge distribution provides a useful benchmark to compare against. For the cesium-iodide detector our predictions were systematically larger, but shell model results were comparatively lower than from the electric-charge distribution form factors. This is likely due to the slightly larger charge radius predicted from the shell model, which causes coherence to be lost to a greater extent (for a given momentum transfer). For the argon detector our result is systematically lower than COHERENT's prediction, in contrast to our increased cross section prediction. As with the argon cross sections, the different form factors all produce very similar results because argon-40 is an even-even nucleus.

It is worth noting that the reduction in the theoretical uncertainty achieved for our cross section predictions has essentially no effect on the total uncertainty of our event rate predictions, since they are dominated by the uncertainty in the neutrino flux.

VI. CONCLUSION

In this work we have computed precise flux-averaged cross section predictions for the CEvNS experiments being carried out by the COHERENT collaboration using argon, germanium and cesium-iodide targets. These predictions were made using both Skyme-Hartree-Fock calculations of weak radii, and shell model calculations of nuclear structure factors. The shell model results included sub-leading nuclear effects such as from spin-orbit coupling and axial currents. We used the Skyme-Hartree-Fock calculation to provide a cross-check of the density distribution obtained with the shell model. The results for the F_M response showed very good agreement between these two methods.

Our results are in broad agreement with prior work but have substantially reduced the theoretical errors by up to a factor of 10. Future advances on the experimental side will both reduce the uncertainty on the neutrino flux and increase the number of detected CEvNS events, reducing statistical errors. Combined with these future advancements, our results will pave the way for CEvNS to serve as a precision test of the Standard Model.

ACKNOWLEDGEMENTS

We are grateful to Daniel Pershey, Jacob Zettlemoyer and Oleksandr Tomalak for useful discussions. This work was supported by the Australian Research Council through Discovery Project DP220101727. The work of JLN is supported by the Australian Research Council through the ARC Centre of Excellence for Dark Matter Particle Physics, CE200100008.

Appendix A: Point-like nucleon distributions

Full results for the point-like distribution of nucleons in each nuclear target are given in the tables below. The SHF results were used to construct Fermi-form factors for the Weak-charge distribution. The shell model results are given for comparison only and are not used for any subsequent calculations. The shell model point-nucleon radii were calculated using

$$R_p^2 = -\frac{6}{Z} \frac{dF_p^M(\mathbf{q}^2)}{d\mathbf{q}^2} \Big|_{\mathbf{q}^2=0}, \quad (\text{A1})$$

$$\begin{aligned} M_{JM}(q\vec{x}) &\equiv j_J(qx)Y_{JM}(\Omega_x), \\ \Sigma'_{JM}(q\vec{x}) &\equiv -i \left[\frac{\vec{\nabla}}{q} \times \vec{M}_{JJ}^M(q\vec{x}) \right] \cdot \vec{\sigma}_N = [J]^{-1} \left[-\sqrt{J} \vec{M}_{JJ+1}^M(q\vec{x}) + \sqrt{J+1} \vec{M}_{JJ-1}^M(q\vec{x}) \right] \cdot \vec{\sigma}_N, \\ \Phi''_{JM}(q\vec{x}) &\equiv i \left(\frac{\vec{\nabla}}{q} M_{JM}(q\vec{x}) \right) \cdot \left(\vec{\sigma}_N \times \frac{1}{q} \vec{\nabla} \right), \end{aligned} \quad (\text{C1})$$

where $\vec{M}_{JL}^M \equiv j_L(qx)\vec{Y}_{JLM}$, $[J] = \sqrt{2J+1}$, and $\vec{\sigma}_N$ is the nucleon spin operator. Here, $j_J(qx)$ is the spherical Bessel function, Y_{JM} is the spherical harmonic, and \vec{Y}_{JLM} is the vector spherical harmonic.

The Wigner-Eckart theorem has been used to express matrix elements in reduced form, using the convention

with an equivalent form for the neutrons.

Appendix B: Comparison to nuclear observables

Here we compare experimental nuclear observables to the theoretical shell model values, namely the nuclear energy levels, as well as the magnetic dipole and electric quadrupole moments and transitions. For each of these observables, we provide the values for ^{40}Ar , $^{70,72,74,76}\text{Ge}$ and ^{133}Cs below, whilst the ^{73}Ge and ^{127}I comparisons can be found in [39].

1. Argon-40

2. Germanium-70,72,74,76

3. Cesium-133

Appendix C: EFT/Nuclear Operators

The nuclear operators employed in Eq. (23) have the form

$$\langle j' m' | T_{JM} | j m \rangle = (-1)^{j'-m'} \begin{pmatrix} j' & J & j \\ -m' & M & m \end{pmatrix} \langle j' || T_J || j \rangle. \quad (\text{C2})$$

The one-nucleon matrix elements in Eq. (25) have analytic expressions of the form [15]:

$$\begin{aligned} \langle n' l' \frac{1}{2} j' || M_J || n l \frac{1}{2} j \rangle &= \langle n' l' | j_J(qr_i) | n l \rangle (-1)^{j+1/2+J} \sqrt{\frac{1}{4\pi}} [(2j'+1)(2j+1)]^{\frac{1}{2}} [(2J+1)(2l+1)(2l'+1)]^{\frac{1}{2}} \\ &\times \begin{pmatrix} l' & J & l \\ 0 & 0 & 0 \end{pmatrix} \left\{ \begin{matrix} l' & j' & 1/2 \\ j & l & J \end{matrix} \right\}, \end{aligned} \quad (\text{C3})$$

TABLE VI: Skyrme-Hartree-Fock predictions of root mean square point like proton and neutron radii.

Nucleus	Interaction	R_p (fm)	R_n (fm)
^{40}Ar	SkM*	3.356	3.445
	SLy6	3.330	3.412
	SV-min	3.321	3.418
	UNEDF1	3.296	3.407
	<i>Average</i>	3.326(25)	3.420(17)
^{70}Ge	SkM*	3.949	4.003
	SLy6	3.944	3.988
	SV-min	3.922	3.980
	UNEDF1	3.904	3.975
	<i>Average</i>	3.930(21)	3.986(12)
^{72}Ge	SkM*	3.965	4.053
	SLy6	3.959	4.031
	SV-min	3.940	4.031
	UNEDF1	3.922	4.028
	<i>Average</i>	3.946(20)	4.036(12)
^{73}Ge	SkM*	3.973	4.077
	SLy6	3.965	4.054
	SV-min	3.947	4.054
	UNEDF1	3.931	4.053
	<i>Average</i>	3.954(19)	4.059(11)
^{74}Ge	SkM*	3.980	4.099
	SLy6	3.976	4.081
	SV-min	3.955	4.077
	UNEDF1	3.941	4.078
	<i>Average</i>	3.963(18)	4.084(10)
^{76}Ge	SkM*	4.016	4.163
	SLy6	4.004	4.138
	SV-min	3.978	4.129
	UNEDF1	3.975	4.140
	<i>Average</i>	3.993(20)	4.143(14)
^{127}I	SkM*	4.702	4.836
	SLy6	4.698	4.824
	SV-min	4.676	4.814
	UNEDF1	4.676	4.822
	<i>Average</i>	4.688(14)	4.824(9)
^{133}Cs	SkM*	4.763	4.898
	SLy6	4.759	4.885
	SV-min	4.739	4.878
	UNEDF1	4.740	4.887
	<i>Average</i>	4.750(12)	4.887(8)

$$\begin{aligned}
\langle n'l' \frac{1}{2} j' \parallel j_{J'}(pr_i) [Y_{J'}(\hat{\mathbf{r}}_i) \boldsymbol{\sigma}_i]^J \parallel nl \frac{1}{2} j \rangle &= \langle n'l' | j_{J'}(qr_i) | nl \rangle (-1)^{l'} \sqrt{\frac{6}{4\pi}} [(2l' + 1)(2l + 1)(2j' + 1)(2j + 1)]^{\frac{1}{2}} \\
&\times [(2J' + 1)(2J + 1)]^{\frac{1}{2}} \begin{pmatrix} l' & J' & l \\ 0 & 0 & 0 \end{pmatrix} \begin{Bmatrix} l' & l & J' \\ 1/2 & 1/2 & 1 \\ j' & j & J \end{Bmatrix}, \tag{C4}
\end{aligned}$$

TABLE VII: Shell model predictions of the point-proton, point-neutron and weak radii, using the various shell model calculations for each of the isotopes considered. GCN5082* and SN100PN* refer to GCN5082 Expanded and SN100PN Expanded, respectively.

Nucleus	Interaction	R_p (fm)	R_n (fm)	R_w (fm)
^{40}Ar	SDPF-NR	3.32852	3.43528	3.53293
	SDPF-U	3.32852	3.43528	3.53282
	SDPF-MU	3.32851	3.43528	3.53243
	EPQQM	3.32851	3.43528	3.53348
^{70}Ge	GCN2850	3.95524	4.05401	4.13886
	JUN45	3.95843	4.05818	4.14331
	jj44b	3.95963	4.07061	4.15307
^{72}Ge	GCN2850	3.97233	4.07882	4.16942
	JUN45	3.97412	4.11049	4.19586
	jj44b	3.97457	4.12156	4.20457
^{73}Ge	GCN2850	3.97979	4.11144	4.20019
	JUN45	3.98047	4.13135	4.21644
	jj44b	3.97981	4.14185	4.22461
^{74}Ge	GCN2850	3.98664	4.14437	4.23118
	JUN45	3.98951	4.16453	4.24903
	jj44b	3.98955	4.17113	4.25434
^{76}Ge	GCN2850	4.00136	4.20041	4.28574
	JUN45	4.00456	4.21257	4.29678
	jj44b	4.00422	4.21636	4.29966
^{127}I	B&D	4.6651	4.89861	4.97959
	SN100PN	4.66554	4.92354	4.99969
	Trun. SN100PN	4.66559	4.92575	5.00184
	GCN5082	4.66544	4.91281	4.98982
	GCN5082*	4.66425	4.91304	4.98979
^{133}Cs	SN100PN	4.72559	4.99394	5.06814
	SN100PN*	4.7252	4.99335	5.06752
	GCN5082	4.72545	4.99188	5.06646
	GCN5082*	4.72493	4.99011	5.06455

TABLE VIII: Magnetic dipole and electric quadrupole moments, and electric quadrupole [B(E2)] and magnetic dipole [B(M1)] transitions, between low-lying states of ^{40}Ar . Experimental transition values from [56], while moments taken from [57, 58].

State	Q [efm^2]					μ [n.m.]				
	SDPF-NR	SDPF-U	SDPF-MU	EPQQM	Exp.	SDPF-NR	SDPF-U	SDPF-MU	EPQQM	Exp.
2_1^+	8.30	9.01	10.59	-0.27	+1(4)	-0.401	-0.456	-0.741	0.103	-0.04(6)
	B(E2) [e^2fm^4]					B(M1) [n.m. ²]				
$2_1^+ \rightarrow 0_{gs}^+$	50.31	48.86	46.33	59.58	73.13(325)					
$2_2^+ \rightarrow 0_{gs}^+$	8.024	10.40	7.671	7.294	9.670(1463)					
$0_2^+ \rightarrow 2_1^+$	6.980	14.50	14.68	0.03158	43.07(650)					
$2_2^+ \rightarrow 2_1^+$	23.76	17.83	28.13	60.55	146.26(4063)	0.2710	0.3055	0.2952	0.1203	0.06623(1074)

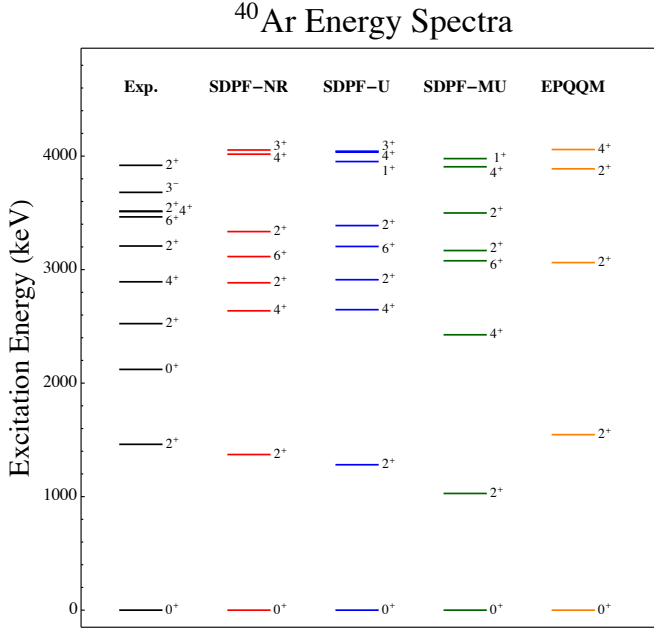


FIG. 5: Experimental energy levels (keV) for ^{40}Ar compared with levels from the SDPF-NR, SDPF-U, SDPF-MU and EPQQM shell model calculations.

TABLE IX: Magnetic dipole and electric quadrupole moments, for low-lying states of $^{70,72,74,76}\text{Ge}$. Experimental moments taken from [57–59].

State	^{70}Ge						^{72}Ge					
	Q [efm ²]			μ [n.m.]			Q [efm ²]			μ [n.m.]		
	JUN45	jj44b	Exp.	JUN45	jj44b	Exp.	JUN45	jj44b	Exp.	JUN45	jj44b	Exp.
2^+_{11}	+14.32	+21.35	+3(6)	+0.72	+0.59	+0.64(10)	+18.30	+15.70	-13(6)	+0.62	+0.52	+0.56(8)
2^+_{22}	-18.63	-21.70		+1.3	+1.1	+1.0(4)	-19.09	-16.14		+1.4	+1.0	+0.5(3)
4^+_{11}	+4.03	+6.48		+1.32	+1.12	+0.88(124)	+13.53	+5.98		+1.12	+0.67	+1.0(3)
	^{74}Ge						^{76}Ge					
2^+_{11}	+16.99	-7.22	-19(2)	+0.59	+0.61	+0.56(8)	+2.99	-18.81	-19(6)	+0.737	+0.596	+0.53(8)
2^+_{22}	-16.13	+6.67	-26(6)	+1.25	+0.96	+0.75(15)	-0.72	+20.20		+1.16	+1.07	+0.64(10)
4^+_{11}	+16.89	-10.15		+0.81	+0.91	+1.3(4)	-0.76	-18.06		+1.20	+0.87	+0.8(6)

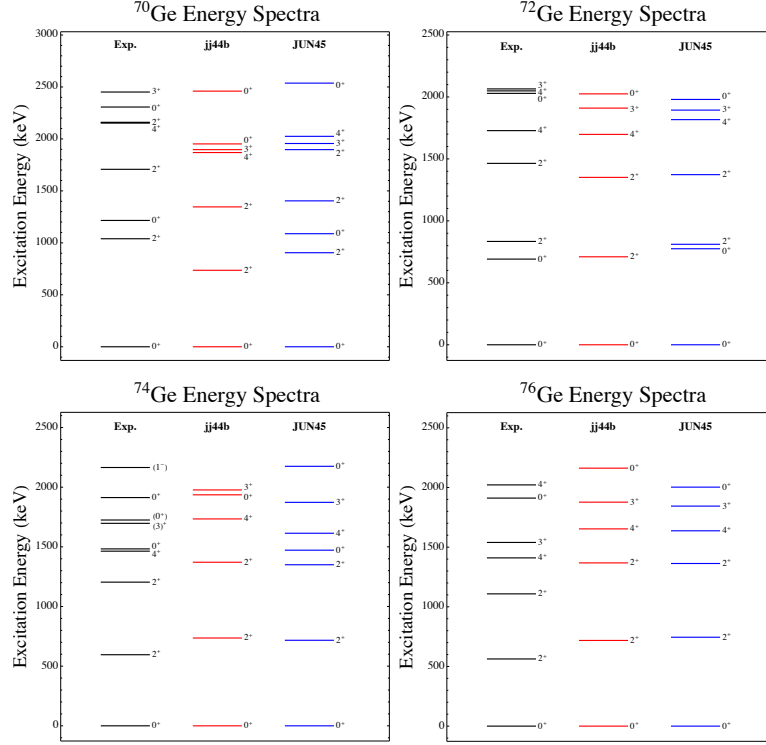


FIG. 6: Low-lying experimental energy levels (keV) for germanium isotopes compared with levels from shell model calculations using the JUN45 and jj44b interactions.

TABLE X: Electric quadrupole [B(E2)] transitions between low-lying states of $^{70,72,74,76}\text{Ge}$. Experimental transitions taken from [60–63].

Transition	^{70}Ge			^{72}Ge			^{74}Ge			^{76}Ge		
	B(E2) [$e^2\text{fm}^4$]			B(E2) [$e^2\text{fm}^4$]			B(E2) [$e^2\text{fm}^4$]			B(E2) [$e^2\text{fm}^4$]		
	JUN45	jj44b	Exp.	JUN45	jj44b	Exp.	JUN45	jj44b	Exp.	JUN45	jj44b	Exp.
$2_1^+ \rightarrow 0_{\text{gs}}^+$	437.3	602.4	356.4(69)	462.6	632.0	418.1(71)	542.8	648.3	609.0(74)	544.8	608.0	550.9(40)
$0_2^+ \rightarrow 2_1^+$	475.9	104.7	822.5(1199)									
$2_2^+ \rightarrow 0_{\text{gs}}^+$	16.80	41.54	8.57(137)	30.22	35.65	2.31($^{+32}_{-43}$)	35.88	2.897	13.1(20)	11.53	0.4896	14.2($^{+15}_{-13}$)
$2_1^+ \rightarrow 0_2^+$				116.0	25.3	316.7(53)						
$4_1^+ \rightarrow 2_1^+$							772.7	885.4	756.6(554)	738.3	809.7	698.0(153)

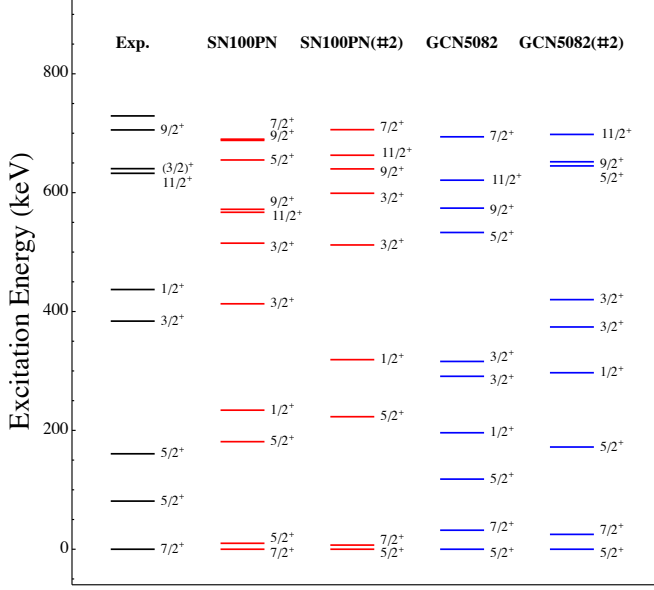
^{133}Cs Energy Spectra

FIG. 7: Experimental energy levels (keV) for ^{133}Cs , compared with levels from SN100PN and GCN5082 shell model calculations for two different valence space truncations.

TABLE XI: Magnetic dipole and electric quadrupole moments for low-lying states of ^{133}Cs . Experimental moments taken from [57, 58, 64]. GCN5082* and SN100PN* refer to GCN5082 Expanded and SN100PN Expanded, respectively.

State	Q [efm^2]					μ [n.m.]				
	SN100PN	SN100PN*	GCN5082	GCN5082*	Exp.	SN100PN	SN100PN*	GCN5082	GCN5082*	Exp.
$7/2_{gs}^+$	-14.11	-13.28	-18.71	-17.13	-0.343(10)	2.6649	2.6880	2.6715	2.7222	+2.5778(14)
$5/2_1^+$	-66.40	-67.47	-63.36	-60.36	30(2) ^a	3.54	3.62	3.36	3.50	+3.45(2)
$5/2_2^+$						2.22	2.19	2.38	2.33	+2.25(15)

^a Sign not specified

TABLE XII: Electric quadrupole [B(E2)] and magnetic dipole [B(M1)] transitions between low-lying states of ^{133}Cs . Experimental transition values from [65]. GCN5082* and SN100PN* refer to GCN5082 Expanded and SN100PN Expanded, respectively.

Transition	B(E2) [$e^2\text{fm}^4$]				
	SN100PN	SN100PN*	GCN5082	GCN5082*	Exp.
$5/2_1^+ \rightarrow 7/2_{\text{gs}}^+$	178.7	155.2	242.8	177.2	233.9(161)
$5/2_2^+ \rightarrow 7/2_{\text{gs}}^+$	1772	1863	1715	1752	1153.3(726)
$3/2_1^+ \rightarrow 7/2_{\text{gs}}^+$	1005	733.5	525.5	217.6	483.9(1210)
B(M1) [n.m. ²]					
$5/2_1^+ \rightarrow 7/2_{\text{gs}}^+$	0.000006111	0.00008033	0.0003863	0.0001393	0.00426(4)
$5/2_2^+ \rightarrow 7/2_{\text{gs}}^+$	0.01032	0.004174	0.01096	0.004590	0.00226(14)

$$\begin{aligned}
\langle n'l'j' || \Phi'' || nlj \rangle &= (-1)^{l'} \frac{6}{\sqrt{4\pi}} \sqrt{(2j'+1)(2j+1)(2l'+1)} \\
&\times \left\{ \sqrt{(J+1)(2J+3)} \sum_{L=J}^{J+1} (-1)^{J+L} (2L+1) \begin{Bmatrix} J+1 & 1 & L \\ 1 & J & 1 \end{Bmatrix} \begin{Bmatrix} l' & l & L \\ 1/2 & 1/2 & 1 \\ j' & j & J \end{Bmatrix} \right. \\
&\times \left[\sqrt{(l+1)(2l+3)} \begin{Bmatrix} J+1 & 1 & L \\ l & l' & l+1 \end{Bmatrix} \begin{pmatrix} l' & J+1 & l+1 \\ 0 & 0 & 0 \end{pmatrix} \langle n'l' | j_{J+1}(qr_i) \left(\frac{\partial}{\partial(qr_i)} - \frac{l}{qr_i} \right) | nl \rangle \right. \\
&\quad \left. - \sqrt{l(2l-1)} \begin{Bmatrix} J+1 & 1 & L \\ l & l' & l-1 \end{Bmatrix} \begin{pmatrix} l' & J+1 & l-1 \\ 0 & 0 & 0 \end{pmatrix} \langle n'l' | j_{J+1}(qr_i) \left(\frac{\partial}{\partial(qr_i)} + \frac{l+1}{qr_i} \right) | nl \rangle \right] \\
&+ \sqrt{J(2J-1)} \sum_{L=J-1}^J (-1)^{J+L} (2L+1) \begin{Bmatrix} J-1 & 1 & L \\ 1 & J & 1 \end{Bmatrix} \begin{Bmatrix} l' & l & L \\ 1/2 & 1/2 & 1 \\ j' & j & J \end{Bmatrix} \\
&\times \left[\sqrt{(l+1)(2l+3)} \begin{Bmatrix} J-1 & 1 & L \\ l & l' & l+1 \end{Bmatrix} \begin{pmatrix} l' & J-1 & l+1 \\ 0 & 0 & 0 \end{pmatrix} \langle n'l' | j_{J-1}(qr_i) \left(\frac{\partial}{\partial(qr_i)} - \frac{l}{qr_i} \right) | nl \rangle \right. \\
&\quad \left. - \sqrt{l(2l-1)} \begin{Bmatrix} J-1 & 1 & L \\ l & l' & l-1 \end{Bmatrix} \begin{pmatrix} l' & J-1 & l-1 \\ 0 & 0 & 0 \end{pmatrix} \langle n'l' | j_{J-1}(qr_i) \left(\frac{\partial}{\partial(qr_i)} + \frac{l+1}{qr_i} \right) | nl \rangle \right] \Big\}.
\end{aligned} \tag{C5}$$

Appendix D: Form factors

In this section we plot the form factors for the individual responses M , Φ'' and Σ' using the shell model calculations performed in this work, where the Σ' response is only plotted for isotopes with non-zero nuclear ground state spin. This is presented for ^{40}Ar , $^{70,72,73,74,76}\text{Ge}$, ^{127}I , and ^{133}Cs , highlighting the corresponding COHERENT range of interest for each of these nuclei. The form factor expressions employed to plot these are presented in [39], except for ^{133}Cs which is provided in Appendix D 8. The KN and SHF form factors were plotted using $(ZF(q, r_{\text{rms}}^p) + NF(q, r_{\text{rms}}^n))^2$, while the shell model counterparts were plotted using $\sum_{N,N'=p,n} F_{X,X}^{(N,N')}(q^2)$, where $F_{X,X}^{(N,N')}(q^2)$ is defined in Eq. (D1).

1. Argon-40

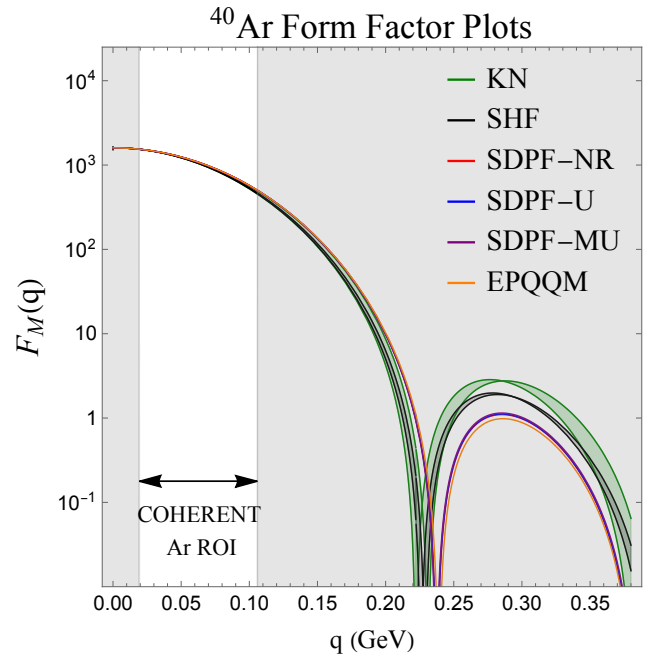


FIG. 8: SI (M) form factors employing the different shell

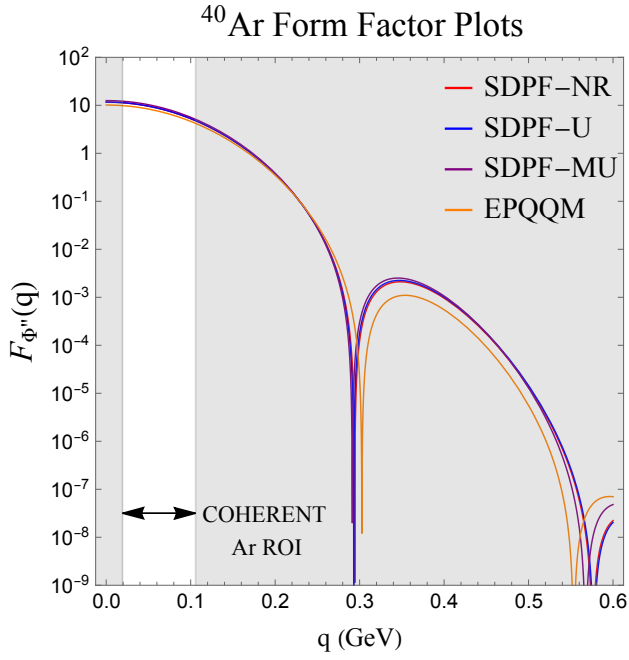


FIG. 9: Φ'' form factors employing the different shell model interactions used for this isotope, plotted against the COHERENT range-of-interest.

2. Germanium-70

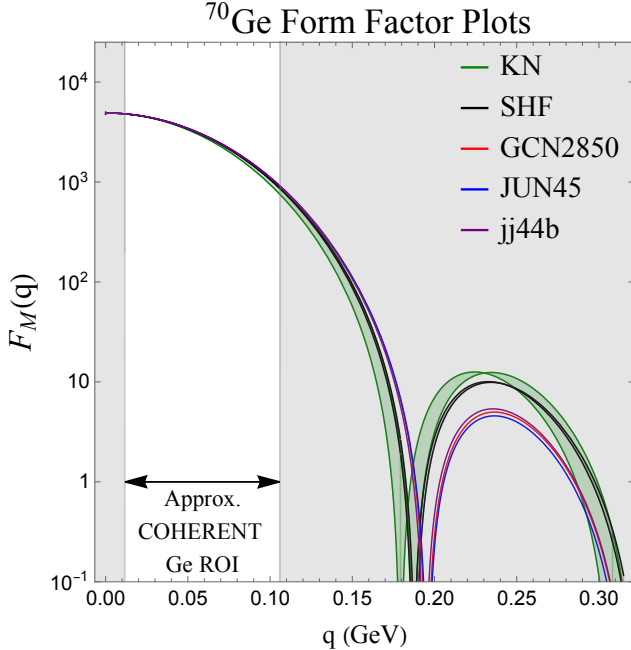


FIG. 10: SI (M) form factors employing the different shell model interactions used for this isotope. This response is compared against the KN and SHF distributions, where the uncertainty bands stem from the r_{rms}^n uncertainty. The COHERENT range-of-interest is also displayed.

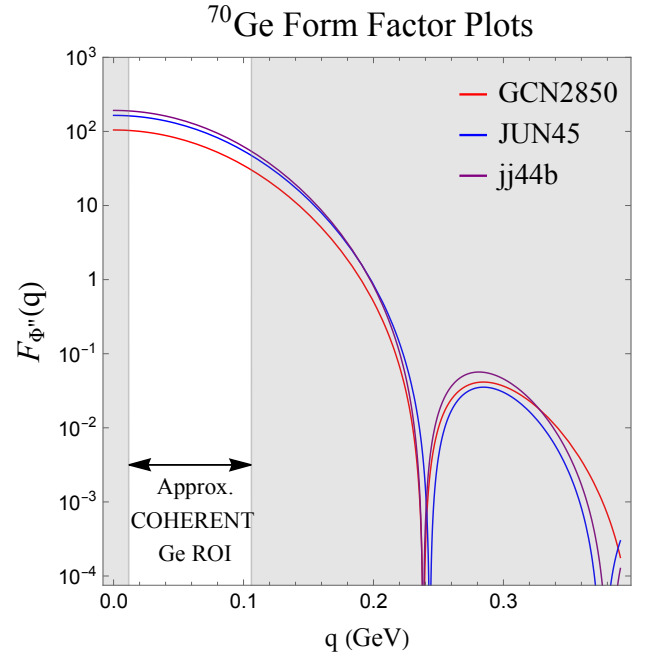


FIG. 11: Φ'' form factors employing the different shell model interactions used for this isotope, plotted against the COHERENT range-of-interest.

3. Germanium-72

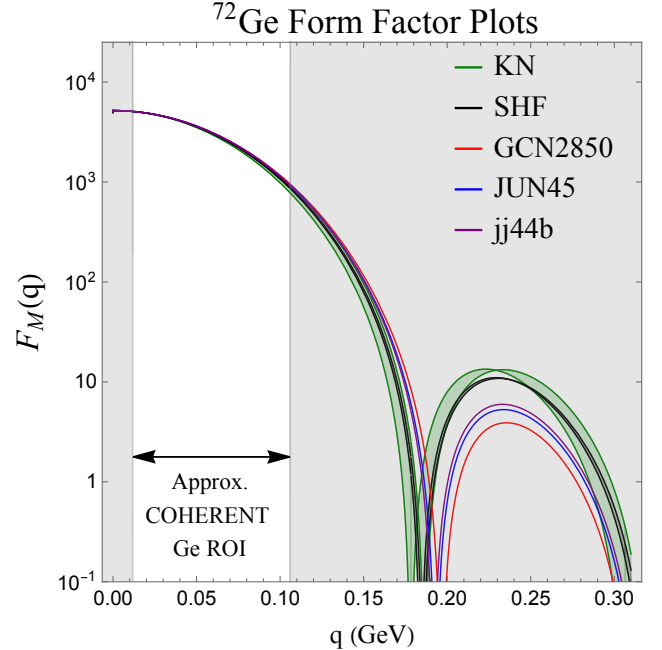


FIG. 12: SI (M) form factors employing the different shell model interactions used for this isotope. This response is compared against the KN and SHF distributions, where the uncertainty bands stem from the r_{rms}^n uncertainty. The COHERENT range-of-interest is also displayed.

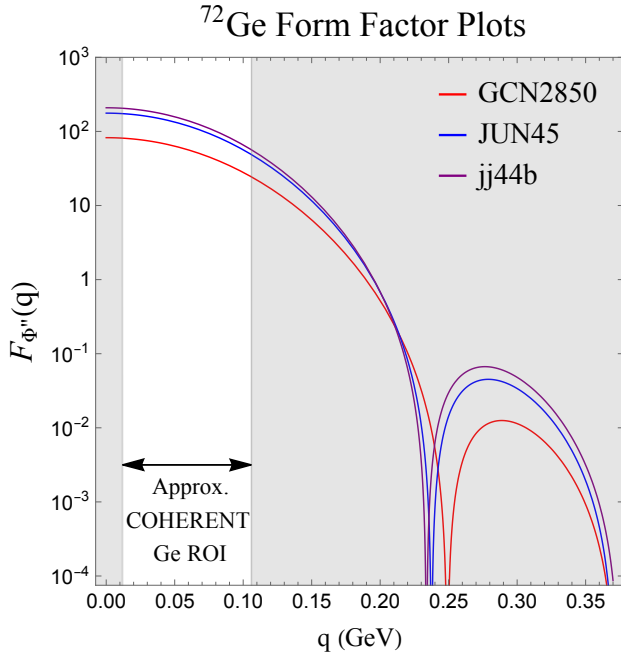


FIG. 13: Φ'' form factors employing the different shell model interactions used for this isotope, plotted against the COHERENT range-of-interest.

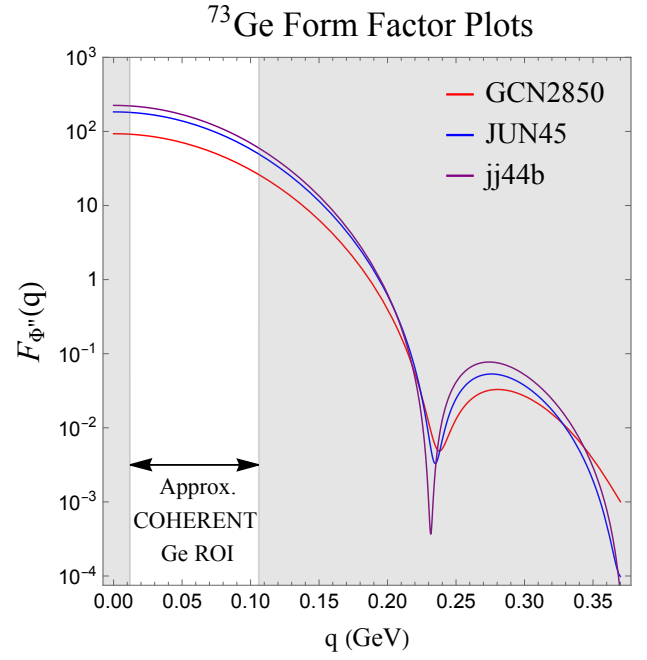


FIG. 15: Φ'' form factors employing the different shell model interactions used for this isotope, plotted against the COHERENT range-of-interest.

4. Germanium-73

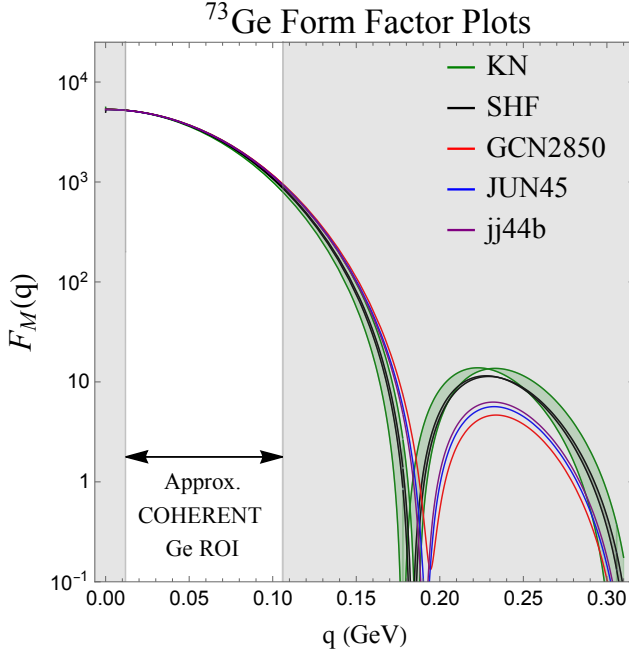


FIG. 14: SI (M) form factors employing the different shell model interactions used for this isotope. This response is compared against the KN and SHF distributions, where the uncertainty bands stem from the r_{rms}^n uncertainty. The COHERENT range-of-interest is also displayed.

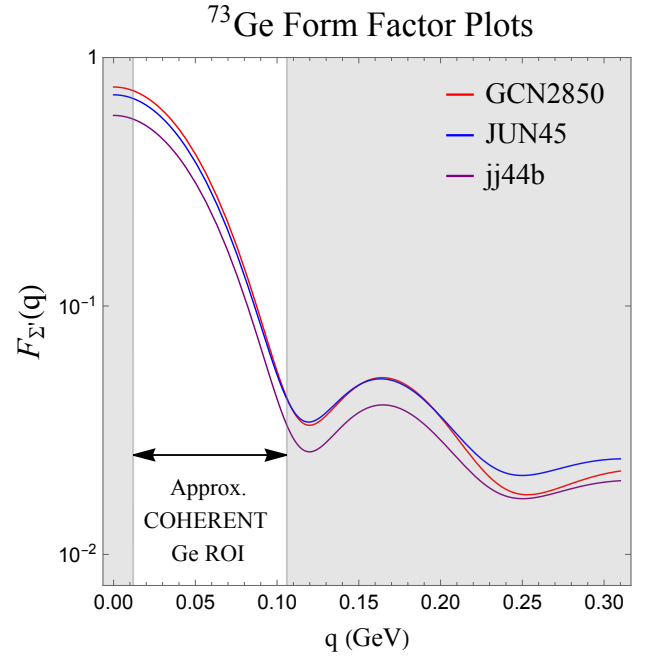


FIG. 16: Σ' form factors employing the different shell model interactions used for this isotope, plotted against the COHERENT range-of-interest.

5. Germanium-74

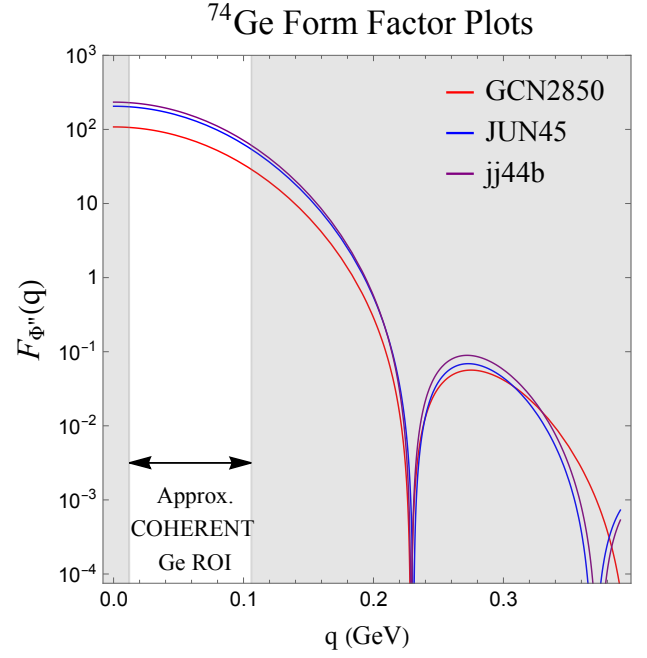


FIG. 18: Φ'' form factors employing the different shell model interactions used for this isotope, plotted against the COHERENT range-of-interest.

6. Germanium-76

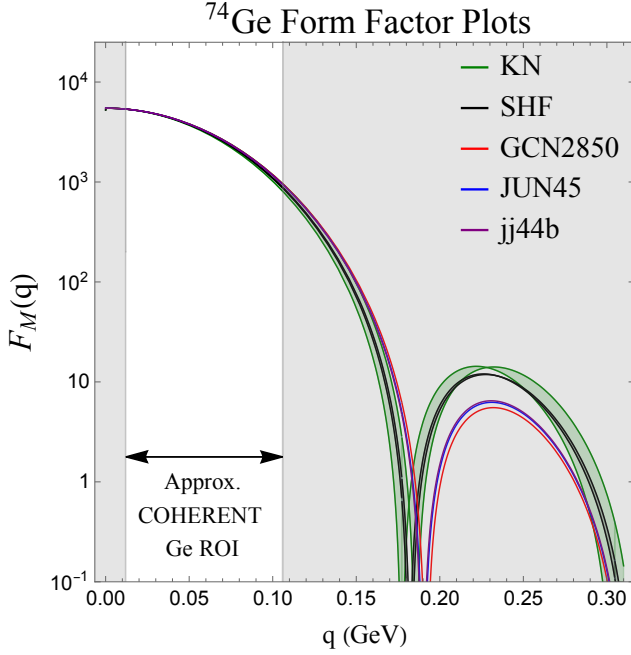


FIG. 17: SI (M) form factors employing the different shell model interactions used for this isotope. This response is compared against the KN and SHF distributions, where the uncertainty bands stem from the r_{rms}^n uncertainty. The COHERENT range-of-interest is also displayed.

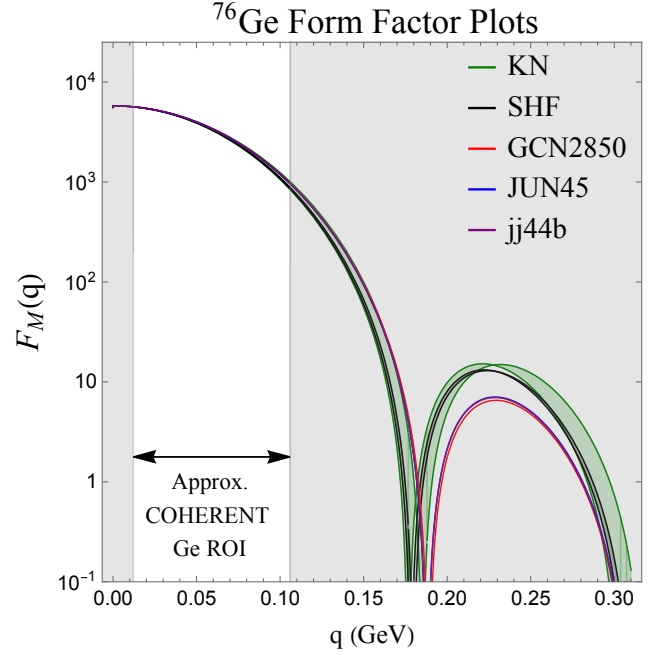


FIG. 19: SI (M) form factors employing the different shell model interactions used for this isotope. This response is compared against the KN and SHF distributions, where the uncertainty bands stem from the r_{rms}^n uncertainty. The COHERENT range-of-interest is also displayed.

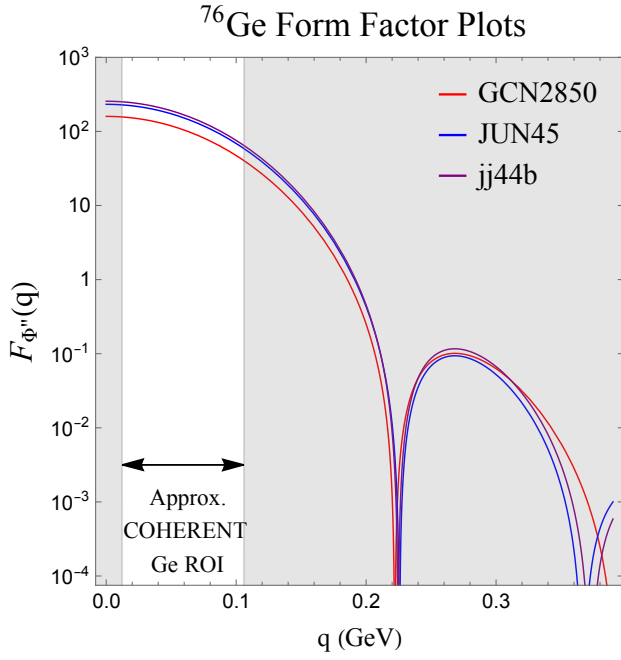


FIG. 20: Φ'' form factors employing the different shell model interactions used for this isotope, plotted against the COHERENT range-of-interest.

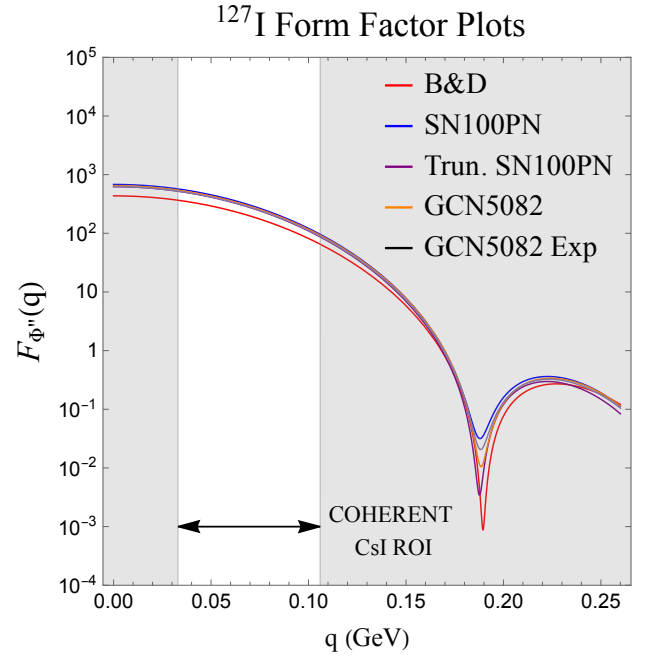


FIG. 22: Φ'' form factors employing the different shell model interactions used for this isotope, plotted against the COHERENT range-of-interest.

7. Iodine-127

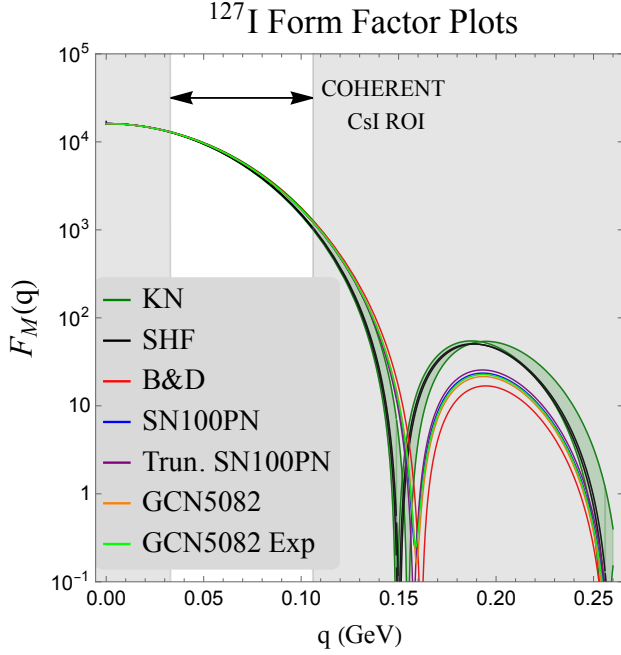


FIG. 21: SI (M) form factors employing the different shell model interactions used for this isotope. This response is compared against the KN and SHF distributions, where the uncertainty bands stem from the r_{rms}^n uncertainty. The COHERENT range-of-interest is also displayed.

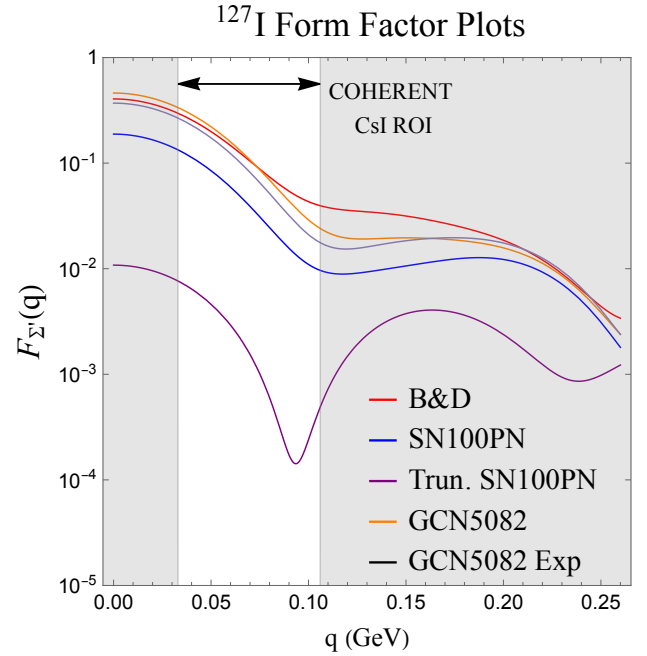


FIG. 23: Σ' form factors employing the different shell model interactions used for this isotope, plotted against the COHERENT range-of-interest.

8. Cesium-133

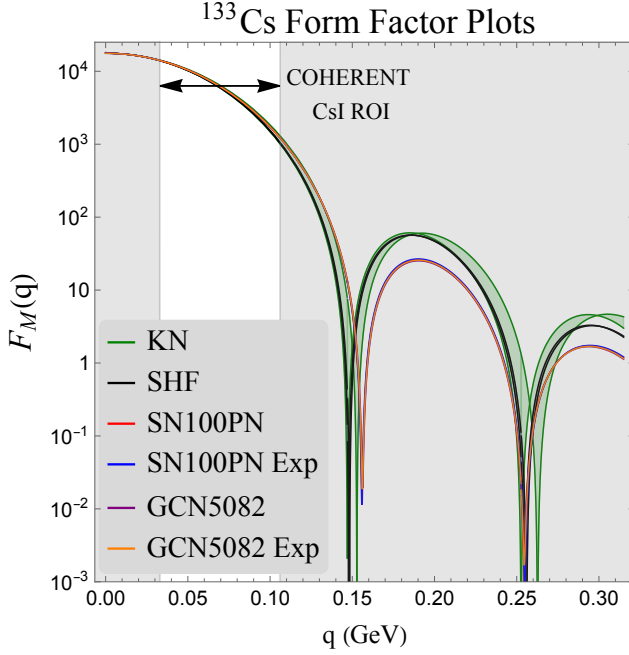


FIG. 24: SI (M) form factors employing the different shell model interactions used for this isotope. This response is compared against the KN and SHF distributions, where the uncertainty bands stem from the r_{rms}^n uncertainty. The COHERENT range-of-interest is also displayed.

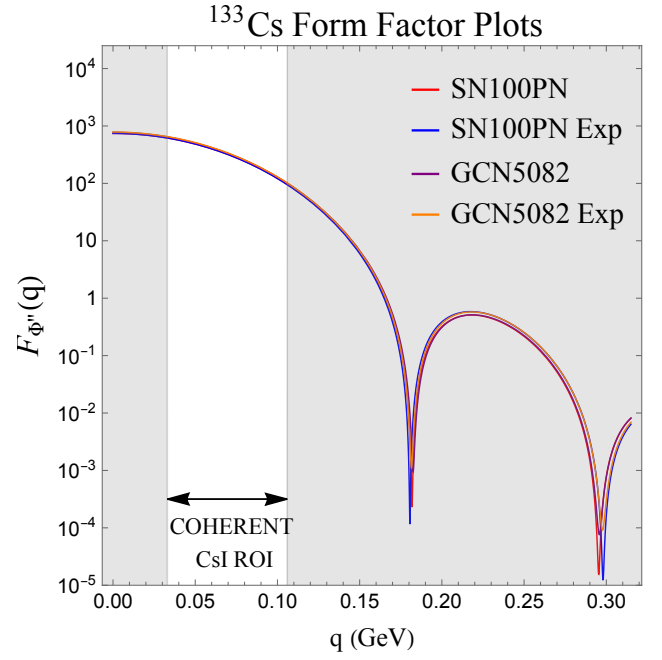


FIG. 25: Φ'' form factors employing the different shell model interactions used for this isotope, plotted against the COHERENT range-of-interest.

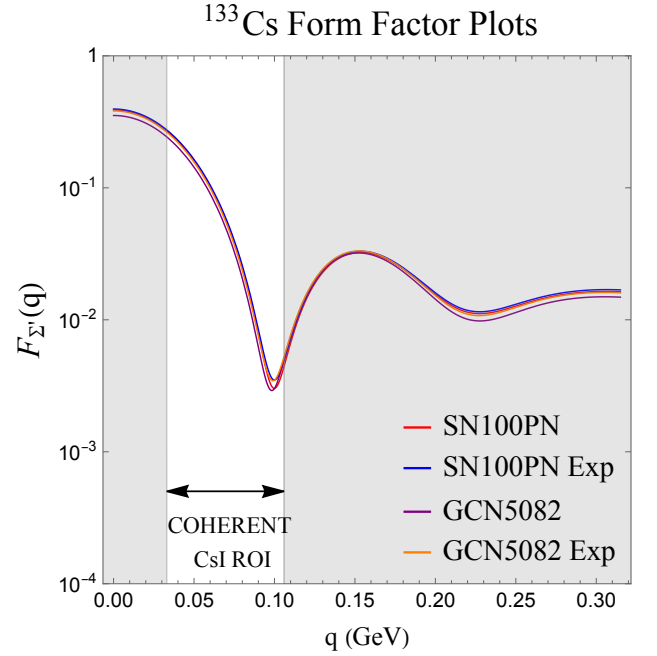


FIG. 26: Σ' form factors employing the different shell model interactions used for this isotope, plotted against the COHERENT range-of-interest.

¹³³Cs Form Factor Expressions

The explicit nuclear form factors for ¹³³Cs are given below using the convention of [35]:

$$F_{X,Y}^{(N,N')}(q^2) \equiv \frac{4\pi}{2J_i + 1} \sum_{J=0}^{2J_i} \langle J_i || X_J^{(N)} || J_i \rangle \langle J_i || Y_J^{(N')} || J_i \rangle, \quad (D1)$$

and can be used to obtain the $\mathcal{F}_N^Y(q^2)$ in Eq. (23). Since no interference occurs between operators in CEvNS, we simplify the notation and write $F_{X,X}^{(N,N')}(q^2) \equiv F_X^{(N,N')}(q^2)$.

SN100PN

$$\begin{aligned}
F_M^{(p,p)} &= e^{-2y}(3020. - 11000.y + 15500.y^2 - 10800.y^3 + 4130.y^4 - 881.y^5 + 103.y^6 - 6.y^7 + 0.145y^8 - 0.000591y^9 + 6.62 \times 10^{-7}y^{10}) \\
F_{\Sigma''}^{(p,p)} &= e^{-2y}(0.204 - 0.18y + 0.0841y^2 + 0.168y^3 - 0.0456y^4 - 0.00246y^5 + 0.014y^6 - 0.00278y^7 + 0.000806y^8 + 1.9 \times 10^{-8}y^9 + 1.19 \times 10^{-12}y^{10}) \\
F_{\Sigma'}^{(p,p)} &= e^{-2y}(0.408 - 3.09y + 8.18y^2 - 9.16y^3 + 5.23y^4 - 1.62y^5 + 0.287y^6 - 0.0273y^7 + 0.00167y^8 + 1.8 \times 10^{-7}y^9 + 2.77 \times 10^{-11}y^{10}) \\
F_{\Phi''}^{(p,p)} &= e^{-2y}(76. - 185.y + 171.y^2 - 75.9y^3 + 17.4y^4 - 2.01y^5 + 0.101y^6 - 0.0012y^7 + 4.14 \times 10^{-6}y^8) \\
F_{\Phi'}^{(p,p)} &= e^{-2y}(0.00327 + 0.00151y - 0.00238y^2 - 0.000124y^3 + 0.00104y^4 - 0.00025y^5 + 0.000026y^6 - 4.22 \times 10^{-9}y^7 + 2.11 \times 10^{-9}y^8) \\
F_{\Delta}^{(p,p)} &= e^{-2y}(2.73 - 6.56y + 6.44y^2 - 2.97y^3 + 0.704y^4 - 0.0813y^5 + 0.00378y^6 - 1.37 \times 10^{-6}y^7 + 1.91 \times 10^{-10}y^8) \\
F_{M\Phi''}^{(p,p)} &= e^{-2y}(-479. + 1460.y - 1680.y^2 + 948.y^3 - 284.y^4 + 45.8y^5 - 3.72y^6 + 0.127y^7 - 0.000979y^8 + 1.66 \times 10^{-6}y^9) \\
F_{\Sigma'\Delta}^{(p,p)} &= e^{-2y}(1.06 - 5.26y + 8.26y^2 - 6.02y^3 + 2.24y^4 - 0.451y^5 + 0.0461y^6 - 0.00218y^7 + 1.81 \times 10^{-8}y^8 + 7.25 \times 10^{-11}y^9) \\
\\
F_M^{(p,n)} &= e^{-2y}(4280. - 17000.y + 26500.y^2 - 20900.y^3 + 9210.y^4 - 2350.y^5 + 342.y^6 - 27.y^7 + 1.y^8 - 0.0128y^9 + 0.000025y^{10}) \\
F_{\Sigma''}^{(p,n)} &= e^{-2y}(-0.0048 + 0.0153y - 0.0323y^2 + 0.0186y^3 + 0.000919y^4 - 0.00533y^5 + 0.00219y^6 - 0.000397y^7 + 0.0000337y^8 - 9.97 \times 10^{-7}y^9 + 1.92 \times 10^{-11}y^{10}) \\
F_{\Sigma'}^{(p,n)} &= e^{-2y}(-0.00961 + 0.0804y - 0.264y^2 + 0.382y^3 - 0.279y^4 + 0.112y^5 - 0.0259y^6 + 0.0034y^7 - 0.000232y^8 + 6.38 \times 10^{-6}y^9 + 8.41 \times 10^{-10}y^{10}) \\
F_{\Phi''}^{(p,n)} &= e^{-2y}(161. - 449.y + 478.y^2 - 252.y^3 + 70.9y^4 - 10.8y^5 + 0.831y^6 - 0.0265y^7 + 0.000156y^8) \\
F_{\Phi'}^{(p,n)} &= e^{-2y}(-0.0171 + 0.0166y + 0.00245y^2 - 0.0105y^3 + 0.00504y^4 - 0.00096y^5 + 0.000072y^6 - 1.28 \times 10^{-6}y^7 - 2.6 \times 10^{-8}y^8) \\
F_{\Delta}^{(p,n)} &= e^{-2y}(0.199 - 0.526y + 0.584y^2 - 0.324y^3 + 0.0954y^4 - 0.0148y^5 + 0.0011y^6 - 0.0000299y^7 + 6.02 \times 10^{-9}y^8) \\
F_{M\Phi''}^{(p,n)} &= e^{-2y}(-1020. + 3440.y - 4510.y^2 + 2950.y^3 - 1060.y^4 + 213.y^5 - 23.6y^6 + 1.31y^7 - 0.0295y^8 + 0.0000625y^9) \\
F_{\Sigma'\Delta}^{(p,n)} &= e^{-2y}(0.0768 - 0.401y + 0.694y^2 - 0.581y^3 + 0.26y^4 - 0.0643y^5 + 0.00865y^6 - 0.000584y^7 + 0.0000155y^8 + 2.25 \times 10^{-9}y^9) \\
\\
F_{M\Phi''}^{(n,p)} &= e^{-2y}(-679. + 2290.y - 2960.y^2 + 1920.y^3 - 680.y^4 + 135.y^5 - 14.5y^6 + 0.749y^7 - 0.0132y^8 + 0.0000625y^9) \\
F_{\Sigma'\Delta}^{(n,p)} &= e^{-2y}(-0.0249 + 0.144y - 0.304y^2 + 0.29y^3 - 0.141y^4 + 0.0379y^5 - 0.00559y^6 + 0.000415y^7 - 0.0000118y^8 + 2.25 \times 10^{-9}y^9) \\
\\
F_M^{(n,n)} &= e^{-2y}(6070. - 26100.y + 44600.y^2 - 39200.y^3 + 19700.y^4 - 5870.y^5 + 1040.y^6 - 106.y^7 + 5.58y^8 - 0.124y^9 + 0.000948y^{10}) \\
F_{\Sigma''}^{(n,n)} &= e^{-2y}(0.000113 - 0.00062y + 0.00352y^2 - 0.00581y^3 + 0.00463y^4 - 0.00205y^5 + 0.00053y^6 - 0.0000795y^7 + 6.33 \times 10^{-6}y^8 - 2.1 \times 10^{-7}y^9 + 2.77 \times 10^{-9}y^{10}) \\
F_{\Sigma'}^{(n,n)} &= e^{-2y}(0.000226 - 0.00207y + 0.00999y^2 - 0.018y^3 + 0.0157y^4 - 0.00743y^5 + 0.00209y^6 - 0.000355y^7 + 0.0000357y^8 - 1.84 \times 10^{-6}y^9 + 3.92 \times 10^{-8}y^{10}) \\
F_{\Phi''}^{(n,n)} &= e^{-2y}(343. - 1070.y + 1300.y^2 - 797.y^3 + 269.y^4 - 51.4y^5 + 5.41y^6 - 0.287y^7 + 0.00593y^8)
\end{aligned}$$

$$\begin{aligned}
F_{\Phi'}^{(n,n)} &= e^{-2y}(0.0891 - 0.215y + 0.223y^2 - 0.122y^3 + 0.038y^4 - 0.00687y^5 + 0.000686y^6 - 0.0000332y^7 + 6.04 \times 10^{-7}y^8) \\
F_{\Delta}^{(n,n)} &= e^{-2y}(0.0144 - 0.0417y + 0.0517y^2 - 0.0334y^3 + 0.012y^4 - 0.00238y^5 + 0.000252y^6 - 0.0000128y^7 + 2.54 \times 10^{-7}y^8) \\
F_{M\Phi''}^{(n,n)} &= e^{-2y}(-1440. + 5360.y - 7780.y^2 + 5760.y^3 - 2400.y^4 + 578.y^5 - 80.2y^6 + 6.04y^7 - 0.213y^8 + 0.00237y^9) \\
F_{\Sigma\Delta}^{(n,n)} &= e^{-2y}(-0.00181 + 0.0109y - 0.0246y^2 + 0.0263y^3 - 0.015y^4 + 0.00482y^5 - 0.000901y^6 + 0.0000936y^7 - 4.82 \times 10^{-6}y^8 + 9.94 \times 10^{-8}y^9)
\end{aligned}$$

SN100PN Expanded

$$\begin{aligned}
F_M^{(p,p)} &= e^{-2y}(3020. - 11000.y + 15500.y^2 - 10800.y^3 + 4120.y^4 - 876.y^5 + 102.y^6 - 5.91y^7 + 0.143y^8 - 0.000608y^9 + 7.17 \times 10^{-7}y^{10}) \\
F_{\Sigma''}^{(p,p)} &= e^{-2y}(0.206 - 0.19y + 0.1y^2 + 0.166y^3 - 0.0494y^4 + 0.000185y^5 + 0.0135y^6 - 0.00271y^7 + 0.000818y^8 + 2.12 \times 10^{-8}y^9 + 1.62 \times 10^{-12}y^{10}) \\
F_{\Sigma'}^{(p,p)} &= e^{-2y}(0.412 - 3.11y + 8.21y^2 - 9.17y^3 + 5.21y^4 - 1.61y^5 + 0.283y^6 - 0.0269y^7 + 0.00167y^8 + 2.15 \times 10^{-7}y^9 + 3.99 \times 10^{-11}y^{10}) \\
F_{\Phi'}^{(p,p)} &= e^{-2y}(75.3 - 184.y + 170.y^2 - 75.5y^3 + 17.3y^4 - 2.01y^5 + 0.102y^6 - 0.00125y^7 + 4.48 \times 10^{-6}y^8) \\
F_{\Phi'}^{(p,p)} &= e^{-2y}(0.0028 + 0.00224y - 0.00221y^2 - 0.000663y^3 + 0.00134y^4 - 0.000307y^5 + 0.0000285y^6 + 1.9 \times 10^{-8}y^7 + 2.31 \times 10^{-9}y^8) \\
F_{\Delta}^{(p,p)} &= e^{-2y}(2.77 - 6.65y + 6.53y^2 - 3.01y^3 + 0.713y^4 - 0.0822y^5 + 0.00382y^6 - 1.66 \times 10^{-6}y^7 + 2.77 \times 10^{-10}y^8) \\
F_{M\Phi''}^{(p,p)} &= e^{-2y}(-477. + 1450.y - 1670.y^2 + 944.y^3 - 283.y^4 + 45.6y^5 - 3.71y^6 + 0.126y^7 - 0.00101y^8 + 1.79 \times 10^{-6}y^9) \\
F_{\Sigma\Delta}^{(p,p)} &= e^{-2y}(1.07 - 5.31y + 8.33y^2 - 6.06y^3 + 2.25y^4 - 0.452y^5 + 0.046y^6 - 0.00217y^7 + 1.65 \times 10^{-8}y^8 + 1.05 \times 10^{-10}y^9) \\
F_M^{(p,n)} &= e^{-2y}(4280. - 17000.y + 26500.y^2 - 20800.y^3 + 9180.y^4 - 2330.y^5 + 339.y^6 - 26.7y^7 + 0.998y^8 - 0.013y^9 + 0.0000266y^{10}) \\
F_{\Sigma''}^{(p,n)} &= e^{-2y}(-0.0042 + 0.0114y - 0.0194y^2 + 0.00958y^3 + 0.00118y^4 - 0.00307y^5 + 0.00117y^6 - 0.000213y^7 + 0.00002y^8 - 7.23 \times 10^{-7}y^9 + 1.64 \times 10^{-11}y^{10}) \\
F_{\Sigma'}^{(p,n)} &= e^{-2y}(-0.00841 + 0.0695y - 0.22y^2 + 0.309y^3 - 0.219y^4 + 0.0848y^5 - 0.0189y^6 + 0.00241y^7 - 0.000163y^8 + 4.55 \times 10^{-6}y^9 + 7.28 \times 10^{-10}y^{10}) \\
F_{\Phi''}^{(p,n)} &= e^{-2y}(161. - 449.y + 479.y^2 - 252.y^3 + 70.9y^4 - 10.8y^5 + 0.84y^6 - 0.0273y^7 + 0.000166y^8) \\
F_{\Phi'}^{(p,n)} &= e^{-2y}(-0.0115 + 0.00924y + 0.00526y^2 - 0.00957y^3 + 0.00411y^4 - 0.00075y^5 + 0.0000598y^6 - 1.43 \times 10^{-6}y^7 - 2.15 \times 10^{-8}y^8) \\
F_{\Delta}^{(p,n)} &= e^{-2y}(0.18 - 0.468y + 0.513y^2 - 0.285y^3 + 0.0835y^4 - 0.0127y^5 + 0.000896y^6 - 0.0000218y^7 + 5.22 \times 10^{-9}y^8) \\
F_{M\Phi''}^{(p,n)} &= e^{-2y}(-1020. + 3460.y - 4530.y^2 + 2960.y^3 - 1060.y^4 + 213.y^5 - 23.6y^6 + 1.32y^7 - 0.0299y^8 + 0.0000666y^9) \\
F_{\Sigma\Delta}^{(p,n)} &= e^{-2y}(0.0695 - 0.359y + 0.608y^2 - 0.506y^3 + 0.226y^4 - 0.0552y^5 + 0.00718y^6 - 0.000457y^7 + 0.000011y^8 + 1.95 \times 10^{-9}y^9) \\
F_{M\Phi''}^{(n,p)} &= e^{-2y}(-675. + 2280.y - 2950.y^2 + 1910.y^3 - 677.y^4 + 134.y^5 - 14.5y^6 + 0.752y^7 - 0.0136y^8 + 0.0000666y^9) \\
F_{\Sigma\Delta}^{(n,p)} &= e^{-2y}(-0.0218 + 0.124y - 0.253y^2 + 0.234y^3 - 0.11y^4 + 0.0286y^5 - 0.00409y^6 + 0.000299y^7 - 8.57 \times 10^{-6}y^8 + 1.95 \times 10^{-9}y^9) \\
F_M^{(n,n)} &= e^{-2y}(6060. - 26100.y + 44600.y^2 - 39200.y^3 + 19600.y^4 - 5840.y^5 + 1030.y^6 - 105.y^7 + 5.58y^8 - 0.127y^9 + 0.000994y^{10}) \\
F_{\Sigma''}^{(n,n)} &= e^{-2y}(0.0000858 - 0.000388y + 0.00137y^2 - 0.00192y^3 + 0.00139y^4 - 0.000568y^5 + 0.000138y^6 - 0.0000202y^7 + 1.72 \times 10^{-6}y^8 - 7.53 \times 10^{-8}y^9 + 1.43 \times 10^{-9}y^{10}) \\
F_{\Sigma'}^{(n,n)} &= e^{-2y}(0.000172 - 0.00154y + 0.0061y^2 - 0.0102y^3 + 0.0086y^4 - 0.00401y^5 + 0.00112y^6 - 0.000189y^7 + 0.0000185y^8 - 9.03 \times 10^{-7}y^9 + 2.03 \times 10^{-8}y^{10}) \\
F_{\Phi''}^{(n,n)} &= e^{-2y}(344. - 1080.y + 1310.y^2 - 803.y^3 + 270.y^4 - 51.5y^5 + 5.45y^6 - 0.293y^7 + 0.00621y^8) \\
F_{\Phi'}^{(n,n)} &= e^{-2y}(0.0471 - 0.113y + 0.115y^2 - 0.0603y^3 + 0.0179y^4 - 0.00312y^5 + 0.000316y^6 - 0.0000171y^7 + 3.82 \times 10^{-7}y^8)
\end{aligned}$$

$$\begin{aligned}
F_{\Delta}^{(n,n)} &= e^{-2y}(0.0117 - 0.0328y + 0.0397y^2 - 0.0256y^3 + 0.00922y^4 - 0.0018y^5 + 0.000179y^6 - 7.73 \times 10^{-6}y^7 + 1.32 \times 10^{-7}y^8) \\
F_{M\Phi''}^{(n,n)} &= e^{-2y}(-1440. + 5380.y - 7820.y^2 + 5780.y^3 - 2400.y^4 + 577.y^5 - 80.2y^6 + 6.07y^7 - 0.217y^8 + 0.00248y^9) \\
F_{\Sigma'\Delta}^{(n,n)} &= e^{-2y}(-0.00142 + 0.00836y - 0.0178y^2 + 0.0182y^3 - 0.0101y^4 + 0.00319y^5 - 0.000576y^6 + 0.0000566y^7 - 2.65 \times 10^{-6}y^8 + 5.16 \times 10^{-8}y^9)
\end{aligned}$$

GCN5082

$$\begin{aligned}
F_M^{(p,p)} &= e^{-2y}(3020. - 11000.y + 15500.y^2 - 10900.y^3 + 4220.y^4 - 914.y^5 + 109.y^6 - 6.58y^7 + 0.165y^8 - 0.000663y^9 + 7.35 \times 10^{-7}y^{10}) \\
F_{\Sigma''}^{(p,p)} &= e^{-2y}(0.185 - 0.0951y - 0.0302y^2 + 0.167y^3 + 0.0107y^4 - 0.0318y^5 + 0.0186y^6 - 0.00298y^7 + 0.000747y^8 + 1.84 \times 10^{-8}y^9 + 2.34 \times 10^{-12}y^{10}) \\
F_{\Sigma'}^{(p,p)} &= e^{-2y}(0.37 - 2.86y + 7.74y^2 - 8.75y^3 + 5.02y^4 - 1.57y^5 + 0.281y^6 - 0.0275y^7 + 0.00167y^8 + 3.2 \times 10^{-7}y^9 + 7.21 \times 10^{-11}y^{10}) \\
F_{\Phi''}^{(p,p)} &= e^{-2y}(92.1 - 225.y + 208.y^2 - 93.y^3 + 21.5y^4 - 2.52y^5 + 0.128y^6 - 0.00143y^7 + 4.59 \times 10^{-6}y^8) \\
F_{\Phi'}^{(p,p)} &= e^{-2y}(0.0147 - 0.00888y + 0.000482y^2 + 0.00251y^3 - (3.38 * 10^{(-6)})y^4 - 0.0000492y^5 + 0.0000216y^6 + 4.51 \times 10^{-7}y^7 + 3.47 \times 10^{-9}y^8) \\
F_{\Delta}^{(p,p)} &= e^{-2y}(2.65 - 6.37y + 6.21y^2 - 2.86y^3 + 0.678y^4 - 0.0785y^5 + 0.00367y^6 - 2.32 \times 10^{-6}y^7 + 5.1 \times 10^{-10}y^8) \\
F_{M\Phi''}^{(p,p)} &= e^{-2y}(-528. + 1600.y - 1850.y^2 + 1050.y^3 - 320.y^4 + 52.3y^5 - 4.34y^6 + 0.15y^7 - 0.00112y^8 + 1.84 \times 10^{-6}y^9) \\
F_{\Sigma'\Delta}^{(p,p)} &= e^{-2y}(0.991 - 5.02y + 7.93y^2 - 5.78y^3 + 2.16y^4 - 0.436y^5 + 0.045y^6 - 0.00214y^7 + 3.71 \times 10^{-8}y^8 + 1.91 \times 10^{-10}y^9)
\end{aligned}$$

$$\begin{aligned}
F_M^{(p,n)} &= e^{-2y}(4280. - 17000.y + 26500.y^2 - 21000.y^3 + 9290.y^4 - 2380.y^5 + 351.y^6 - 28.1y^7 + 1.06y^8 - 0.0135y^9 + 0.0000258y^{10}) \\
F_{\Sigma''}^{(p,n)} &= e^{-2y}(-0.00421 + 0.0148y - 0.029y^2 + 0.0133y^3 + 0.00321y^4 - 0.00556y^5 + 0.0021y^6 - 0.000387y^7 + 0.0000362y^8 - 1.17 \times 10^{-6}y^9 + 2.84 \times 10^{-11}y^{10}) \\
F_{\Sigma'}^{(p,n)} &= e^{-2y}(-0.00841 + 0.0722y - 0.243y^2 + 0.357y^3 - 0.265y^4 + 0.108y^5 - 0.0256y^6 + 0.00346y^7 - 0.000246y^8 + 7.12 \times 10^{-6}y^9 + 1.42 \times 10^{-9}y^{10}) \\
F_{\Phi''}^{(p,n)} &= e^{-2y}(175. - 486.y + 519.y^2 - 274.y^3 + 77.4y^4 - 11.8y^5 + 0.916y^6 - 0.0292y^7 + 0.000162y^8) \\
F_{\Phi'}^{(p,n)} &= e^{-2y}(-0.0389 + 0.0585y - 0.0328y^2 + 0.00374y^3 + 0.00233y^4 - 0.000795y^5 + 0.0000795y^6 - 1.68 \times 10^{-6}y^7 - 4.12 \times 10^{-8}y^8) \\
F_{\Delta}^{(p,n)} &= e^{-2y}(0.223 - 0.588y + 0.643y^2 - 0.351y^3 + 0.102y^4 - 0.0157y^5 + 0.00117y^6 - 0.0000316y^7 + 1.03 \times 10^{-8}y^8) \\
F_{M\Phi''}^{(p,n)} &= e^{-2y}(-1000. + 3390.y - 4440.y^2 + 2920.y^3 - 1050.y^4 + 214.y^5 - 23.9y^6 + 1.35y^7 - 0.031y^8 + 0.0000646y^9) \\
F_{\Sigma'\Delta}^{(p,n)} &= e^{-2y}(0.0832 - 0.441y + 0.762y^2 - 0.632y^3 + 0.28y^4 - 0.0688y^5 + 0.00921y^6 - 0.000627y^7 + 0.000017y^8 + 3.83 \times 10^{-9}y^9)
\end{aligned}$$

$$\begin{aligned}
F_{M\Phi''}^{(n,p)} &= e^{-2y}(-747. + 2520.y - 3260.y^2 + 2120.y^3 - 753.y^4 + 150.y^5 - 16.3y^6 + 0.839y^7 - 0.0144y^8 + 0.0000646y^9) \\
F_{\Sigma'\Delta}^{(n,p)} &= e^{-2y}(-0.0225 + 0.133y - 0.283y^2 + 0.272y^3 - 0.134y^4 + 0.0366y^5 - 0.00553y^6 + 0.000422y^7 - 0.0000125y^8 + 3.83 \times 10^{-9}y^9)
\end{aligned}$$

$$\begin{aligned}
F_M^{(n,n)} &= e^{-2y}(6070. - 26100.y + 44500.y^2 - 39200.y^3 + 19700.y^4 - 5880.y^5 + 1040.y^6 - 106.y^7 + 5.58y^8 - 0.122y^9 + 0.000919y^{10}) \\
F_{\Sigma''}^{(n,n)} &= e^{-2y}(0.0000957 - 0.000626y + 0.0036y^2 - 0.00574y^3 + 0.00447y^4 - 0.00195y^5 + 0.000504y^6 - 0.0000768y^7 + 6.4 \times 10^{-6}y^8 - 2.28 \times 10^{-7}y^9 + 3.28 \times 10^{-9}y^{10}) \\
F_{\Sigma'}^{(n,n)} &= e^{-2y}(0.000191 - 0.0018y + 0.00906y^2 - 0.0167y^3 + 0.0148y^4 - 0.00718y^5 + 0.00205y^6 - 0.000357y^7 + 0.0000371y^8 - 1.98 \times 10^{-6}y^9 + 4.34 \times 10^{-8}y^{10}) \\
F_{\Phi''}^{(n,n)} &= e^{-2y}(333. - 1040.y + 1260.y^2 - 773.y^3 + 261.y^4 - 49.7y^5 + 5.23y^6 - 0.277y^7 + 0.00574y^8) \\
F_{\Phi'}^{(n,n)} &= e^{-2y}(0.103 - 0.247y + 0.254y^2 - 0.137y^3 + 0.0425y^4 - 0.00762y^5 + 0.000756y^6 - 0.0000363y^7 + 6.56 \times 10^{-7}y^8) \\
F_{\Delta}^{(n,n)} &= e^{-2y}(0.0187 - 0.0538y + 0.0652y^2 - 0.0412y^3 + 0.0145y^4 - 0.00283y^5 + 0.000293y^6 - 0.0000145y^7 + 2.79 \times 10^{-7}y^8)
\end{aligned}$$

$$\begin{aligned}
F_{M\Phi''}^{(n,n)} &= e^{-2y}(-1420. + 5270.y - 7660.y^2 + 5670.y^3 - 2360.y^4 + 569.y^5 - 79.y^6 + 5.94y^7 - 0.209y^8 + 0.0023y^9) \\
F_{\Sigma'\Delta}^{(n,n)} &= e^{-2y}(-0.00189 + 0.0116y - 0.026y^2 + 0.0276y^3 - 0.0157y^4 + 0.00509y^5 - 0.000965y^6 + 0.000102y^7 - 5.31 \times 10^{-6}y^8 + 1.1 \times 10^{-7}y^9)
\end{aligned}$$

GCN5082 Expanded

$$\begin{aligned}
F_M^{(p,p)} &= e^{-2y}(3020. - 11000.y + 15500.y^2 - 10900.y^3 + 4200.y^4 - 907.y^5 + 108.y^6 - 6.46y^7 + 0.162y^8 - 0.000701y^9 + 8.42 \times 10^{-7}y^{10}) \\
F_{\Sigma''}^{(p,p)} &= e^{-2y}(0.193 - 0.121y + 0.00697y^2 + 0.175y^3 - 0.00996y^4 - 0.0217y^5 + 0.0172y^6 - 0.0029y^7 + 0.000786y^8 + 3.71 \times 10^{-8}y^9 + 3.42 \times 10^{-12}y^{10}) \\
F_{\Sigma'}^{(p,p)} &= e^{-2y}(0.386 - 2.97y + 7.97y^2 - 8.97y^3 + 5.13y^4 - 1.6y^5 + 0.284y^6 - 0.0276y^7 + 0.0017y^8 + 3.15 \times 10^{-7}y^9 + 8.5 \times 10^{-11}y^{10}) \\
F_{\Phi''}^{(p,p)} &= e^{-2y}(91.3 - 223.y + 207.y^2 - 92.9y^3 + 21.6y^4 - 2.55y^5 + 0.131y^6 - 0.00154y^7 + 5.26 \times 10^{-6}y^8) \\
F_{\Phi'}^{(p,p)} &= e^{-2y}(0.015 - 0.00813y + 0.000808y^2 + 0.00263y^3 - (8.21 * 10^{-6}))y^4 - 0.0000477y^5 + 0.0000242y^6 + 5.25 \times 10^{-7}y^7 + 4.03 \times 10^{-9}y^8) \\
F_{\Delta}^{(p,p)} &= e^{-2y}(2.74 - 6.58y + 6.44y^2 - 2.97y^3 + 0.703y^4 - 0.0812y^5 + 0.00379y^6 - 2.48 \times 10^{-6}y^7 + 5.93 \times 10^{-10}y^8) \\
F_{M\Phi''}^{(p,p)} &= e^{-2y}(-525. + 1600.y - 1850.y^2 + 1050.y^3 - 319.y^4 + 52.3y^5 - 4.34y^6 + 0.151y^7 - 0.00118y^8 + 2.1 \times 10^{-6}y^9) \\
F_{\Sigma'\Delta}^{(p,p)} &= e^{-2y}(1.03 - 5.18y + 8.17y^2 - 5.96y^3 + 2.22y^4 - 0.447y^5 + 0.046y^6 - 0.00218y^7 + 2.02 \times 10^{-8}y^8 + 2.24 \times 10^{-10}y^9)
\end{aligned}$$

$$\begin{aligned}
F_M^{(p,n)} &= e^{-2y}(4280. - 17000.y + 26400.y^2 - 20900.y^3 + 9250.y^4 - 2370.y^5 + 348.y^6 - 27.8y^7 + 1.05y^8 - 0.0137y^9 + 0.0000284y^{10}) \\
F_{\Sigma''}^{(p,n)} &= e^{-2y}(-0.000933 + 0.00115y - 0.00851y^2 + 0.00811y^3 - 0.00352y^4 + 0.0000644y^5 + 0.00036y^6 - 0.000128y^7 + 0.0000185y^8 - 8.1 \times 10^{-7}y^9 + 1.54 \times 10^{-11}y^{10}) \\
F_{\Sigma'}^{(p,n)} &= e^{-2y}(-0.00187 + 0.0274y - 0.124y^2 + 0.206y^3 - 0.16y^4 + 0.0672y^5 - 0.0161y^6 + 0.00221y^7 - 0.000159y^8 + 4.77 \times 10^{-6}y^9 + 1.01 \times 10^{-9}y^{10}) \\
F_{\Phi''}^{(p,n)} &= e^{-2y}(176. - 490.y + 524.y^2 - 276.y^3 + 78.1y^4 - 12.y^5 + 0.935y^6 - 0.0303y^7 + 0.000177y^8) \\
F_{\Phi'}^{(p,n)} &= e^{-2y}(-0.0278 + 0.0407y - 0.0221y^2 + 0.00217y^3 + 0.00162y^4 - 0.000525y^5 + 0.0000548y^6 - 1.43 \times 10^{-6}y^7 - 3.34 \times 10^{-8}y^8) \\
F_{\Delta}^{(p,n)} &= e^{-2y}(0.188 - 0.488y + 0.526y^2 - 0.287y^3 + 0.0828y^4 - 0.0124y^5 + 0.000881y^6 - 0.0000216y^7 + 7.34 \times 10^{-9}y^8) \\
F_{M\Phi''}^{(p,n)} &= e^{-2y}(-1010. + 3430.y - 4490.y^2 + 2940.y^3 - 1060.y^4 + 215.y^5 - 24.y^6 + 1.36y^7 - 0.0314y^8 + 0.0000709y^9) \\
F_{\Sigma'\Delta}^{(p,n)} &= e^{-2y}(0.0706 - 0.37y + 0.625y^2 - 0.512y^3 + 0.225y^4 - 0.0545y^5 + 0.00706y^6 - 0.000454y^7 + 0.0000113y^8 + 2.73 \times 10^{-9}y^9)
\end{aligned}$$

$$\begin{aligned}
F_{M\Phi''}^{(n,p)} &= e^{-2y}(-743. + 2510.y - 3250.y^2 + 2110.y^3 - 751.y^4 + 150.y^5 - 16.3y^6 + 0.848y^7 - 0.015y^8 + 0.0000709y^9) \\
F_{\Sigma'\Delta}^{(n,p)} &= e^{-2y}(-0.00497 + 0.0599y - 0.158y^2 + 0.164y^3 - 0.0838y^4 + 0.0234y^5 - 0.00359y^6 + 0.00028y^7 - 8.51 \times 10^{-6}y^8 + 2.73 \times 10^{-9}y^9)
\end{aligned}$$

$$\begin{aligned}
F_M^{(n,n)} &= e^{-2y}(6050. - 26100.y + 44400.y^2 - 39100.y^3 + 19600.y^4 - 5850.y^5 + 1040.y^6 - 105.y^7 + 5.58y^8 - 0.125y^9 + 0.000963y^{10}) \\
F_{\Sigma''}^{(n,n)} &= e^{-2y}(4.51 \times 10^{-6} - 8.31 \times 10^{-6}y + 0.000803y^2 - 0.00169y^3 + 0.0016y^4 - 0.000798y^5 + 0.000224y^6 - 0.0000347y^7 + 2.67 \times 10^{-6}y^8 - 7.76 \times 10^{-8}y^9 + 1.46 \times 10^{-9}y^{10}) \\
F_{\Sigma'}^{(n,n)} &= e^{-2y}(9.02 \times 10^{-6} - 0.000196y + 0.00242y^2 - 0.00533y^3 + 0.00506y^4 - 0.00254y^5 + 0.000758y^6 - 0.000139y^7 + 0.0000153y^8 - 8.33 \times 10^{-7}y^9 + 1.95 \times 10^{-8}y^{10}) \\
F_{\Phi''}^{(n,n)} &= e^{-2y}(339. - 1060.y + 1290.y^2 - 788.y^3 + 265.y^4 - 50.4y^5 + 5.32y^6 - 0.286y^7 + 0.00602y^8) \\
F_{\Phi'}^{(n,n)} &= e^{-2y}(0.0514 - 0.123y + 0.123y^2 - 0.0637y^3 + 0.0189y^4 - 0.00332y^5 + 0.000335y^6 - 0.0000177y^7 + 3.75 \times 10^{-7}y^8) \\
F_{\Delta}^{(n,n)} &= e^{-2y}(0.0129 - 0.036y + 0.0427y^2 - 0.0268y^3 + 0.00939y^4 - 0.0018y^5 + 0.000175y^6 - 7.44 \times 10^{-6}y^7 + 1.25 \times 10^{-7}y^8) \\
F_{M\Phi''}^{(n,n)} &= e^{-2y}(-1430. + 5330.y - 7740.y^2 + 5720.y^3 - 2370.y^4 + 572.y^5 - 79.4y^6 + 6.y^7 - 0.213y^8 + 0.00241y^9)
\end{aligned}$$

$$F_{\Sigma'\Delta}^{(n,n)} = e^{-2y}(-0.000341 + 0.00418y - 0.0111y^2 + 0.0125y^3 - 0.00739y^4 + 0.00247y^5 - 0.000477y^6 + 0.0000503y^7 - 2.49 \times 10^{-6}y^8 + 4.92 \times 10^{-8}y^9)$$

¹³³Cs Occupation Number Table

The occupation numbers n_{nlj}^N of each valence single-nucleon orbital are given in order of increasing orbit, with $N = \{p, n\}$ denoting protons and neutrons respectively, and n begins at 1. “Max Occ” refers to the maximum occupation number allowed for each orbital. GCN5082* and SN100PN* refer to GCN5082 Expanded and SN100PN Expanded, respectively.

n	l	j	Max Occ	SN100PN		SN100PN*		GCN5082		GCN5082*	
				n_{nlj}^p	n_{nlj}^n	n_{nlj}^p	n_{nlj}^n	n_{nlj}^p	n_{nlj}^n	n_{nlj}^p	n_{nlj}^n
1	4	7/2	8	3.32	7.73	3.36	7.75	2.90	7.71	2.96	7.70
2	2	5/2	6	1.04	6.00	1.03	5.67	1.38	6.00	1.35	5.73
2	2	3/2	4	0.23	2.63	0.22	2.77	0.30	2.68	0.27	2.77
3	0	1/2	2	0.14	1.61	0.12	1.51	0.14	1.73	0.12	1.64
1	5	11/2	12	0.26	10.02	0.28	10.28	0.28	9.87	0.30	10.14

- [1] D. Akimov *et al.* (COHERENT), Observation of Coherent Elastic Neutrino-Nucleus Scattering, *Science* **357**, 1123 (2017), arXiv:1708.01294 [nucl-ex].
- [2] D. Akimov *et al.* (COHERENT), First Measurement of Coherent Elastic Neutrino-Nucleus Scattering on Argon, *Phys. Rev. Lett.* **126**, 012002 (2021), arXiv:2003.10630 [nucl-ex].
- [3] I. Bernardi (COHERENT), CEvNS and COHERENT, *PoS NOW2022*, 066 (2023).
- [4] M. Bowen and P. Huber, Reactor neutrino applications and coherent elastic neutrino nucleus scattering, *Phys. Rev. D* **102**, 053008 (2020), arXiv:2005.10907 [physics.ins-det].
- [5] M. Cadeddu, C. Giunti, Y. F. Li, and Y. Y. Zhang, Average CsI neutron density distribution from COHERENT data, *Phys. Rev. Lett.* **120**, 072501 (2018), arXiv:1710.02730 [hep-ph].
- [6] D. K. Papoulias, T. S. Kosmas, R. Sahu, V. K. B. Kota, and M. Hota, Constraining nuclear physics parameters with current and future COHERENT data, *Phys. Lett. B* **800**, 135133 (2020), arXiv:1903.03722 [hep-ph].
- [7] P. Coloma, I. Esteban, M. C. Gonzalez-Garcia, and J. Menendez, Determining the nuclear neutron distribution from Coherent Elastic neutrino-Nucleus Scattering: current results and future prospects, *JHEP* **08** (08), 030, arXiv:2006.08624 [hep-ph].
- [8] I. A. Bisset, B. Dutta, W.-C. Huang, and L. E. Strigari, Short Baseline Neutrino Anomalies at Stopped Pion Experiments, (2023), arXiv:2310.13194 [hep-ph].
- [9] P. B. Denton, Y. Farzan, and I. M. Shoemaker, Testing large non-standard neutrino interactions with arbitrary mediator mass after COHERENT data, *JHEP* **07**, 037, arXiv:1804.03660 [hep-ph].
- [10] P. Coloma, M. C. Gonzalez-Garcia, M. Maltoni, and T. Schwetz, COHERENT Enlightenment of the Neutrino Dark Side, *Phys. Rev. D* **96**, 115007 (2017), arXiv:1708.02899 [hep-ph].
- [11] J. B. Dent, B. Dutta, S. Liao, J. L. Newstead, L. E. Strigari, and J. W. Walker, Accelerator and reactor complementarity in coherent neutrino-nucleus scattering, *Phys. Rev. D* **97**, 035009 (2018), arXiv:1711.03521 [hep-ph].
- [12] T. S. Kosmas, D. K. Papoulias, M. Tórtola, and J. W. F. Valle, Probing light sterile neutrino signatures at reactor and spallation neutron source neutrino experiments, *Phys. Rev. D* **96**, 063013 (2017).
- [13] S. Al Kharusi *et al.* (SNEWS), SNEWS 2.0: a next-generation supernova early warning system for multimessenger astronomy, *New J. Phys.* **23**, 031201 (2021), arXiv:2011.00035 [astro-ph.HE].
- [14] D. Akimov *et al.* (COHERENT), A D₂O detector for flux normalization of a pion decay-at-rest neutrino source, *JINST* **16** (08), P08048, arXiv:2104.09605 [physics.ins-det].
- [15] M. Hoferichter, J. Menéndez, and A. Schwenk, Coherent elastic neutrino-nucleus scattering: Eft analysis and nuclear responses, *Phys. Rev. D* **102**, 074018 (2020).
- [16] C. G. Payne, S. Bacca, G. Hagen, W. Jiang, and T. Papenbrock, Coherent elastic neutrino-nucleus scattering on ⁴⁰Ar from first principles, *Phys. Rev. C* **100**, 061304 (2019), arXiv:1908.09739 [nucl-th].
- [17] B. Dutta, W.-C. Huang, J. L. Newstead, and V. Pandey, Inelastic nuclear scattering from neutrinos and dark matter, *Phys. Rev. D* **106**, 113006 (2022), arXiv:2206.08590 [hep-ph].
- [18] B. Dutta, W.-C. Huang, and J. L. Newstead, Probing the Dark Sector with Nuclear Transition Photons, *Phys. Rev. Lett.* **131**, 111801 (2023), arXiv:2302.10250 [hep-ph].
- [19] D. Z. Freedman, Coherent effects of a weak neutral current, *Phys. Rev. D* **9**, 1389 (1974).
- [20] J. D. Lewin and P. F. Smith, Review of mathematics, numerical factors, and corrections for dark matter experiments based on elastic nuclear recoil, *Astropart. Phys.* **6**, 87 (1996).
- [21] S. R. Klein and J. Nystrand, Exclusive vector meson production in relativistic heavy ion collisions, *Phys. Rev. C* **60**, 014903 (1999).
- [22] D. Aristizabal Sierra, J. Liao, and D. Marfatia, Impact of form factor uncertainties on interpretations of coherent elastic neutrino-nucleus scattering data, *JHEP* **06**, 141, arXiv:1902.07398 [hep-ph].
- [23] O. Tomalak, P. Machado, V. Pandey, and R. Plestid, Flavor-dependent radiative corrections in coherent elastic neutrino-nucleus scattering, *JHEP* **02**, 097, arXiv:2011.05960 [hep-ph].
- [24] J. Barranco, O. G. Miranda, and T. I. Rashba, Probing new physics with coherent neutrino scattering off nuclei, *JHEP* **12**, 021, arXiv:hep-ph/0508299.
- [25] J. B. Dent, B. Dutta, S. Liao, J. L. Newstead, L. E. Strigari, and J. W. Walker, Probing light mediators at ultralow threshold energies with coherent elastic neutrino-nucleus scattering, *Phys. Rev. D* **96**, 095007 (2017), arXiv:1612.06350 [hep-ph].
- [26] B. Reed, Z. Jaffe, C. J. Horowitz, and C. Sfienti, Measuring the surface thickness of the weak charge density of nuclei, *Phys. Rev. C* **102**, 064308 (2020), arXiv:2009.06664 [nucl-th].
- [27] D. Adhikari *et al.* (PREX), Accurate Determination of the Neutron Skin Thickness of ²⁰⁸Pb through Parity-Violation in Electron Scattering, *Phys. Rev. Lett.* **126**, 172502 (2021), arXiv:2102.10767 [nucl-ex].
- [28] K. S. Kumar (PREX, CREX), Electroweak probe of neutron skins of nuclei, *Annals Phys.* **412**, 168012 (2020).
- [29] S. Orrigo, L. Alvarez-Ruso, and C. Peña-Garay, A new approach to nuclear form factors for direct dark matter searches, *Nuclear and Particle Physics Proceedings* **273-275**, 414 (2016), 37th International Conference on High Energy Physics (ICHEP).
- [30] I. Angeli and K. P. Marinova, Table of experimental nuclear ground state charge radii: An update, *Atom. Data Nucl. Data Tabl.* **99**, 69 (2013).
- [31] P.-G. Reinhard, B. Schuetrumpf, and J. A. Maruhn, The Axial Hartree-Fock + BCS Code SkyAx, *Comput. Phys. Commun.* **258**, 107603 (2021).
- [32] D. W. L. Sprung and J. Martorell, The symmetrized fermi function and its transforms, *Journal of Physics A: Mathematical and General* **30**, 6525 (1997).
- [33] J. S. O'Connell, T. W. Donnelly, and J. D. Walecka, Semileptonic weak interactions with c¹², *Phys. Rev. C* **6**, 719 (1972).
- [34] T. de Forest Jr. and J. Walecka, Electron scattering and nuclear structure, *Advances in Physics* **15**, 1 (1966),

- <https://doi.org/10.1080/00018736600101254>.
- [35] A. L. Fitzpatrick, W. Haxton, E. Katz, N. Lubbers, and Y. Xu, The Effective Field Theory of Dark Matter Direct Detection, *JCAP* **02**, 004, [arXiv:1203.3542](https://arxiv.org/abs/1203.3542) [hep-ph].
- [36] T. Donnelly and W. Haxton, Multipole operators in semileptonic weak and electromagnetic interactions with nuclei: Harmonic oscillator single-particle matrix elements, *Atomic Data and Nuclear Data Tables* **23**, 103 (1979).
- [37] B. A. Brown and W. D. Rae, The Shell-Model Code NuShellX@MSU, *Nuclear Data Sheets* **120**, 115 (2014).
- [38] N. Anand, A. L. Fitzpatrick, and W. C. Haxton, Weakly interacting massive particle-nucleus elastic scattering response, *Phys. Rev. C* **89**, 065501 (2014), [arXiv:1308.6288](https://arxiv.org/abs/1308.6288) [hep-ph].
- [39] R. Abdel Khaleq, G. Busoni, C. Simenel, and A. E. Stuchbery, Impact of shell model interactions on nuclear responses to WIMP elastic scattering, *Phys. Rev. D* **109**, 075036 (2024), [arXiv:2311.15764](https://arxiv.org/abs/2311.15764) [hep-ph].
- [40] S. Nummela, P. Baumann, E. Caurier, P. Dessagne, A. Jokinen, A. Knipper, G. Le Scornet, C. Miehé, F. Nowacki, M. Oinonen, Z. Radivojevic, M. Ramdhane, G. Walter, and J. Äystö, Spectroscopy of $^{34,35}\text{Si}$ by β decay: sd-fp shell gap and single-particle states, *Physical Review C - Nuclear Physics* [10.1103/PhysRevC.63.044316](https://arxiv.org/abs/10.1103/PhysRevC.63.044316) (2001).
- [41] F. Nowacki and A. Poves, New effective interaction for 0ω shell-model calculations in the sd-pf valence space, *Physical Review C - Nuclear Physics* [10.1103/PhysRevC.79.014310](https://arxiv.org/abs/10.1103/PhysRevC.79.014310) (2009).
- [42] K. Kaneko, Y. Sun, T. Mizusaki, and M. Hasegawa, Shell-model study for neutron-rich sd-shell nuclei, *Physical Review C - Nuclear Physics* [10.1103/PhysRevC.83.014320](https://arxiv.org/abs/10.1103/PhysRevC.83.014320) (2011).
- [43] Y. Utsuno, T. Otsuka, B. A. Brown, M. Honma, T. Mizusaki, and N. Shimizu, Shape transitions in exotic Si and S isotopes and tensor-force-driven Jahn-Teller effect, *Physical Review C* [10.1103/physrevc.86.051301](https://arxiv.org/abs/10.1103/physrevc.86.051301) (2012).
- [44] A. E. Stuchbery and J. L. Wood, To shell model, or not to shell model, that is the question, *Physics* **4**, 697 (2022).
- [45] J. Menéndez, A. Poves, E. Caurier, and F. Nowacki, Disassembling the nuclear matrix elements of the neutrinoless $\beta\beta$ decay, *Nuclear Physics A* [10.1016/j.nuclphysa.2008.12.005](https://arxiv.org/abs/10.1016/j.nuclphysa.2008.12.005) (2009).
- [46] M. Honma, T. Otsuka, T. Mizusaki, and M. Hjorth-Jensen, New effective interaction for f5pg9-shell nuclei, *Physical Review C - Nuclear Physics* [10.1103/PhysRevC.80.064323](https://arxiv.org/abs/10.1103/PhysRevC.80.064323) (2009).
- [47] S. Mukhopadhyay, B. P. Crider, B. A. Brown, S. F. Ashley, A. Chakraborty, A. Kumar, M. T. McEllistrem, E. E. Peters, F. M. Prados-Estévez, and S. W. Yates, Nuclear structure of Ge 76 from inelastic neutron scattering measurements and shell model calculations, *Physical Review C* [10.1103/PhysRevC.95.014327](https://arxiv.org/abs/10.1103/PhysRevC.95.014327) (2017).
- [48] W. J. Baldrige and B. J. Dalton, Shell-model studies for the Sn132 region. II. Exact and statistical results for multi-proton cases, *Physical Review C* **18**, 539 (1978).
- [49] B. A. Brown, N. J. Stone, J. R. Stone, I. S. Towner, and M. Hjorth-Jensen, Magnetic moments of the 21^+ states around ^{132}Sn , *Physical Review C* **71**, 044317 (2005).
- [50] D. Akimov *et al.* (COHERENT), Measurement of the Coherent Elastic Neutrino-Nucleus Scattering Cross Section on CsI by COHERENT, *Phys. Rev. Lett.* **129**, 081801 (2022), [arXiv:2110.07730](https://arxiv.org/abs/2110.07730) [hep-ex].
- [51] N. Ackermann *et al.*, Final CONUS results on coherent elastic neutrino nucleus scattering at the Brokdorf reactor, (2024), [arXiv:2401.07684](https://arxiv.org/abs/2401.07684) [hep-ex].
- [52] C. Augier *et al.* (Ricochet), Results from a prototype TES detector for the Ricochet experiment, *Nucl. Instrum. Meth. A* **1057**, 168765 (2023), [arXiv:2304.14926](https://arxiv.org/abs/2304.14926) [physics.ins-det].
- [53] G. Angloher *et al.* (NUCLEUS), Exploring $\text{CE}\nu\text{NS}$ with NUCLEUS at the Chooz nuclear power plant, *Eur. Phys. J. C* **79**, 1018 (2019), [arXiv:1905.10258](https://arxiv.org/abs/1905.10258) [physics.ins-det].
- [54] D. Akimov *et al.* (COHERENT), COHERENT Collaboration data release from the measurements of CsI[Na] response to nuclear recoils, (2023), [arXiv:2307.10208](https://arxiv.org/abs/2307.10208) [physics.ins-det].
- [55] D. Akimov *et al.* (COHERENT), COHERENT Collaboration data release from the first detection of coherent elastic neutrino-nucleus scattering on argon [10.5281/zenodo.3903810](https://arxiv.org/abs/10.5281/zenodo.3903810) (2020), [arXiv:2006.12659](https://arxiv.org/abs/2006.12659) [nucl-ex].
- [56] J. Chen, Nuclear Data Sheets for $A=40$, *Nuclear Data Sheets* **140**, 1 (2017).
- [57] N. J. Stone, *Table of Recommended Nuclear Magnetic Dipole Moments - Part II, Short-lived States*, Tech. Rep. INDC(NDS)-0816 (2020).
- [58] N. J. Stone, *Table of Nuclear Electric Quadrupole Moments*, Tech. Rep. INDC(NDS)-0833 (2021).
- [59] G. Gürdal *et al.*, Measurements of $g(4_1^+, 2_2^+)$ in $^{70,72,74,76}\text{Ge}$: Systematics of low-lying structures in $30 \leq Z \leq 40$ and $30 \leq N \leq 50$ nuclei, *Phys. Rev. C* **88**, 014301 (2013).
- [60] G. Gürdal and E. A. McCutchan, Nuclear Data Sheets for $A = 70$, *Nucl. Data Sheets* **136**, 1 (2016).
- [61] D. Abriola and A. A. Sonzogni, Nuclear Data Sheets for $A = 72$, *Nucl. Data Sheets* **111**, 1 (2010).
- [62] B. Singh and A. R. Farhan, Nuclear Data Sheets for $A = 74$, *Nucl. Data Sheets* **107**, 1923 (2006).
- [63] B. Singh, J. Chen, and A. R. Farhan, Nuclear Structure and Decay Data for $A=76$ Isobars, *Nucl. Data Sheets* **194**, 3 (2024).
- [64] N. J. Stone, *Table of Recommended Nuclear Magnetic Dipole Moments: Part I - Long-lived States*, Tech. Rep. INDC(NDS)-0794 (2019).
- [65] Y. Khazov, A. Rodionov, and F. G. Kondev, Nuclear Data Sheets for $A = 133$, *Nucl. Data Sheets* **112**, 855 (2011).